



Fluid types and their genetic meaning for the BIF-hosted iron ores, Krivoy Rog, Ukraine



Marta Sośnicka^{a,b,*}, Ronald J. Bakker^c, Curt Broman^d, Iain Pitcairn^d, Ihor Paranko^e, Kingsley Burlinson^f

^a AGH University of Science and Technology, Faculty of Geology, Geophysics and Environmental Protection, Department of Economic Geology, al. A. Mickiewicza 30, 30-059 Krakow, Poland

^b Economic Geology Research Institute, School of Geosciences, University of the Witwatersrand, Private Bag 3, 2050 Wits, Johannesburg, South Africa

^c Resource Mineralogy, Department of Applied Geosciences and Geophysics, Montanuniversitaet Leoben, Peter-Tunner-Str. 5, 8700 Leoben, Austria

^d Department of Geological Sciences, Stockholm University, 10691 Stockholm, Sweden

^e Kryvorizkiy National University, Kryvyj Rig, XXII Partyzidzu Str., 11, 50027 Krivoy Rog, Ukraine

^f Burlinson Geochemical Services Pty. Ltd., Darwin, NT, Australia

ARTICLE INFO

Article history:

Received 14 May 2014

Received in revised form 25 November 2014

Accepted 4 December 2014

Available online 9 January 2015

Keywords:

Banded iron formation

BIF

Fluid inclusions

High-grade iron ore

Ore genesis

Krivoy Rog

Kryvyj Rig

ABSTRACT

This paper contributes to the understanding of the genesis of epigenetic, hypogene BIF-hosted iron deposits situated in the eastern part of Ukrainian Shield. It presents new data from the Krivoy Rog iron mining district (Skelevatske–Magnetitove deposit, Frunze underground mine and Balka Severnaya Krasnaya outcrop) and focuses on the investigation of ore genesis through application of fluid inclusion petrography, microthermometry, Raman spectroscopy and baro-acoustic decrepitation of fluid inclusions. The study investigates inclusions preserved in quartz and magnetite associated with the low-grade iron ores (31–37% Fe) and iron-rich quartzites (38–45% Fe) of the Saksaganskaya Suite, as well as magnetite from the locally named high-grade iron ores (52–56% Fe). These high-grade ores resulted from alteration of iron quartzites in the Saksaganskiy thrust footwall (Saksaganskiy tectonic block) and were a precursor to supergene martite, high-grade ores (60–70% Fe). Based on the new data two stages of iron ore formation (metamorphic and metasomatic) are proposed. The metamorphic stage, resulting in formation of quartz veins within the low-grade iron ore and iron-rich quartzites, involved fluids of four different compositions: CO₂-rich, H₂O, H₂O–CO₂(±N₂–CH₄)–NaCl(±NaHCO₃) and H₂O–CO₂(±N₂–CH₄)–NaCl. The salinities of these fluids were relatively low (up to 7 mass% NaCl equiv.) as these fluids were derived from dehydration and decarbonation of the BIF rocks, however the origin of the nahcolite (NaHCO₃) remains unresolved. The minimum P–T conditions for the formation of these veins, inferred from microthermometry are $T_{\min} = 219\text{--}246\text{ }^{\circ}\text{C}$ and $P_{\min} = 130\text{--}158\text{ MPa}$. The baro-acoustic decrepitation analyses of magnetite bands indicated that the low-grade iron ore from the Skelevatske–Magnetitove deposit was metamorphosed at $T = \sim 530\text{ }^{\circ}\text{C}$.

The metasomatic stage post-dated and partially overlapped the metamorphic stage and led to the upgrade of iron quartzites to the high-grade iron ores. The genesis of these ores, which are located in the Saksaganskiy tectonic block (Saksaganskiy ore field), and the factors controlling iron ore-forming processes are highly controversial. According to the study of quartz-hosted fluid inclusions from the thrust zone the metasomatic stage involved at least three different episodes of the fluid flow, simultaneous with thrusting and deformation. During the 1st episode three types of fluids were introduced: CO₂–CH₄–N₂(±C), CO₂(±N₂–CH₄) and low salinity H₂O–N₂–CH₄–NaCl (6.38–7.1 mass% NaCl equiv.). The 2nd episode included expulsion of the aqueous fluids H₂O–N₂–CH₄–NaCl(±CO₂, ±C) of moderate salinities (15.22–16.76 mass% NaCl equiv.), whereas the 3rd event involved high salinity fluids H₂O–NaCl(±C) (20–35 mass% NaCl equiv.). The fluids most probably interacted with country rocks (e.g. schists) supplying them with CH₄ and N₂. The high salinity fluids were most likely either magmatic–hydrothermal fluids derived from the Saksaganskiy igneous body or heated basinal brines, and they may have caused pervasive leaching of Fe from metavolcanic and/or the BIF rocks. The baro-acoustic decrepitation analyses of magnetite comprising the high-grade iron ore showed formation $T = \sim 430\text{--}500\text{ }^{\circ}\text{C}$. The fluid inclusion data suggest that the upgrade to high-grade Fe ores might be a result of the Krivoy Rog BIF alteration by multiple flows of structurally controlled, metamorphic and magmatic–hydrothermal fluids or heated basinal brines.

© 2015 Elsevier B.V. All rights reserved.

* Corresponding author at: Economic Geology Research Institute EGRI, School of Geosciences, University of the Witwatersrand, Private Bag 3, 2050 Wits, Johannesburg, South Africa.

E-mail address: sosnickamarta@gmail.com (M. Sośnicka).

1. Introduction

Iron ore deposits within Precambrian banded iron formations (BIFs) are the most profitable sources of iron making them very attractive exploration targets (Duuring et al., 2012). However there are many aspects of their genesis and evolution that are controversial and not fully understood, not least the mechanisms of iron ore enrichment, which have been a subject of recent intense research (e.g. Rosière and Rios, 2004; Hagemann et al., 2006; Belykh et al., 2007; Beukes et al., 2008; Spier et al., 2008; Thorne et al., 2009; Angerer et al., 2012; Figueiredo e Silva et al., 2013).

Recently improved genetic models for Fe deposits hosted by BIFs worldwide, e.g. Kursk Group, KMA, Russia (~2.39 Ga), Brockman Iron Formation, Hamersley Basin, Australia (~2.46 Ga), itabirites of the Cauê Formation, Brazil (~2.45 Ga) or Serra Norte Carajás BIF, Brazil (~2.7 Ga) are primarily focused on a direct transition from a BIF-protolith to the high-grade (>58% Fe) martite and hematite ores (e.g. Belykh et al., 2007; Spier et al., 2008; Thorne et al., 2009; Figueiredo e Silva et al., 2013). According to these models the ore-forming fluids, interacting with the BIF-protolith, played a crucial role in the iron ore enrichment (Belykh et al., 2007; Spier et al., 2008; Thorne et al., 2009; Figueiredo e Silva et al., 2013). For instance, martite and specular hematite–martite, high-grade ores from Fe deposits of the KMA region, which are hosted by BIF similar in age and tectonostratigraphic setting to the Krivoy Rog BIF, were upgraded during the introduction of meteoric waters and unknown hypogene fluids derived from deep-seated sources (Belykh et al., 2007). The most recent fluid flow models worldwide also propose multiple interactions of BIF with fluids of various origins, e.g. hypogene and supergene meteoric fluids in Fe deposits of the Quadrilátero Ferrífero region, Brazil (Spier et al., 2008), supergene and modified hydrothermal fluids in deposits of the Iron Ore Group, India (Beukes et al., 2008), basinal brines and meteoric fluids in Hamersley-type deposits, Australia (Hagemann et al., 2006; Thorne et al., 2009) or modified magmatic and meteoric fluids in the Carajás Fe deposits, Brazil (Figueiredo e Silva et al., 2013).

The study by Rosière and Rios (2004) indicated that the ore-forming processes preceding formation of the final product, i.e. high-grade hematite Fe ore, were also not restricted to a single fluid alteration event affecting a parent BIF. They proposed that in Fe deposits of the Quadrilátero Ferrífero district, Brazil, magnetite mineralization predating the transformation to a high-grade hematite ore, resulted from contraction accompanied by influx of reduced metamorphic fluids and connate water (Rosière and Rios, 2004). Belevtsev et al. (1991) describe epigenetic, magnetite, quartz-absent BIF (52–56% Fe) as a proto-ore for the porous, dispersed-hematite–martite, high-grade Fe ores (60–70% Fe) hosted by the BIF of the Krivoy Rog Belt (KRB). This paper aims to unravel the processes behind the formation of Fe ore precursors generated before the enrichment to the supergene dispersed-hematite–martite, high-grade ores. Fe ore precursors include metamorphosed low-grade Fe ore (31–37% Fe) and iron-rich quartzites (38–45% Fe) as well as compacted, quartz-absent Fe ore (52–56% Fe), which is locally named massive, high-grade ore (Belevtsev et al., 1991). These ore types are actively exploited in the KRB in numerous mines, even at depths exceeding 1.3 km. The rocks of KRB have undergone a very complex evolution with multiple metamorphic, metasomatic and magmatic–hydrothermal events, extensive deformation and supergene alteration (Bobrov et al., 2002). Consequently, the generation of high-grade iron ores in this region is not fully understood. The current genetic model relies on the assumption that contraction and partial BIF leaching by hydrothermal fluids of metamorphic origin were responsible for the hypogene iron ore upgrade to epigenetic, compacted high-grade ore, 52–56% Fe (Belevtsev et al., 1991), however an influence of fluids from other sources has been neither confirmed nor excluded (Lazarenko et al., 1977). Unraveling the fluid evolution within the Fe deposits at Krivoy Rog

is crucial to understanding the origin of these ore bodies and could lead to improved genetic models and increased exploration success in the area.

The purpose of this study is to characterize the fluids that formed the iron ores at Krivoy Rog through analysis of fluid inclusions. We use microthermometry and laser Raman techniques on a series of quartz veins and breccias from the low-grade and high-grade iron ores as well as acoustic decrepitation on ore minerals in order to constrain the composition and source of fluids involved in formation of the iron ores.

2. Geology of the Krivoy Rog Belt

The KRB is situated within the Ukrainian Shield close to the border between two geological units, the Paleoproterozoic Kirovogradskiy terrane and the Archean Middle Dniprean (Dnyepropyetrovskiy) terrane (Bobrov et al., 2002; Yesipchuk et al., 2004) (Fig. 1A). The KRB forms an elongated structure, which is constrained by the deep-seated Krivoy Rog–Kremenchug fault zone to the west and the Saksaganskiy and Demurinskiy granitoid massifs to the east (Fig. 1B). The Mesoarchean age of the Saksaganskiy granitoids is 3.067 ± 0.081 Ga (Yesipchuk et al., 2004; Stepanyuk et al., 2010), however the time span of their formation is unknown. The currently valid stratigraphy of the region and of the Krivoy Rog Belt itself is constantly under debate and requires actualization (Paranko et al., 2005; Khudur, 2006; Paranko et al., 2011).

The KRB hosts the Paleoproterozoic Krivoy Rog Series (equivalent of the Supergroup), which comprises six Suites (corresponding to Groups): the Novokrivorozhskaya Suite, the Skelevatskaya Suite, the metakomatiite rock association, the iron ore-bearing Saksaganskaya Suite, the Gdantsevskaya Suite and the Gleyevatskaya Suite (Figs. 1B, 2a, b) (Bobrov et al., 2002; Yesipchuk et al., 2004). The Krivoy Rog Series is underlain by the oldest metavolcanic rocks of the KRB, the Konkskaya Series (Figs. 1B, 2a, b) (Bobrov et al., 2002).

The Novokrivorozhskaya and Skelevatskaya Suites (Figs. 1B, 2a, b) represent metaconglomerate–schist and metaconglomerate–sandstone–schist rock associations, respectively (Bobrov et al., 2002). The metakomatiite rock association (Figs. 1B, 2a, b) is represented by fissure type rocks, and effusive ultramafic lava flows, which were metamorphosed to talc–carbonate schists (Paranko and Mikhnikskaya, 1991; Paranko, 1993; Paranko et al., 1993; Khudur, 2006; Pieczonka et al., 2011). This suite has a thickness of up to 150 m and extends throughout the entire length of the KRB, yet its origin is still unclear (Paranko and Mikhnikskaya, 1991). Its contact with the Skelevatskaya Suite is gradational, whereas the upper boundary is associated with thrust zones (Paranko and Mikhnikskaya, 1991). The Saksaganskaya Suite (Figs. 1B, 2a, b) of a thickness up to 1500 m (Shcherbak and Bobrov, 2005) comprises seven sets of alternating schist and BIF horizons (Fig. 3) (Bobrov et al., 2002). The former are composed of ferruginous schists and barren quartzites, whereas the latter consist of banded ferruginous quartzites (e.g. silicate–magnetite quartzites, jaspilites, locally containing tiger-eye variety) and high-grade iron ores (Paranko and Mikhnikskaya, 1991; Bobrov et al., 2002) (Fig. 4). In the late Paleoproterozoic the rocks of the Saksaganskaya Suite underwent extensive deformation including folding, faulting, metamorphism, thrusting and metasomatism (Bobrov et al., 2002). The metamorphic grades vary from garnet zone greenschist facies at $T = 430\text{--}550$ °C in the central part of the KRB and staurolite-bearing epidote–amphibolite facies at $T = 510\text{--}600$ °C in the southern and northern parts of the KRB (Belevtsev et al., 1983, 1991). The Saksaganskaya Suite is unconformably overlain by the Gdantsevskaya Suite (1400 m) and the Gleyevatskaya Suite (1500–2000 m) (Figs. 1B, 2a, b) (Paranko and Mikhnikskaya, 1991; Paranko, 1993, 1997; Bobrov et al., 2002).

The Archean Konkskaya Series and Paleoproterozoic Krivoy Rog Series (Novokrivorozhskaya–Saksaganskaya Suites) dip to the west and form a monoclinical structure, which is crosscut by thrust zones (Kalyayev et al., 1984; Paranko, 1993; Reshetnyak, 1993; Bobrov

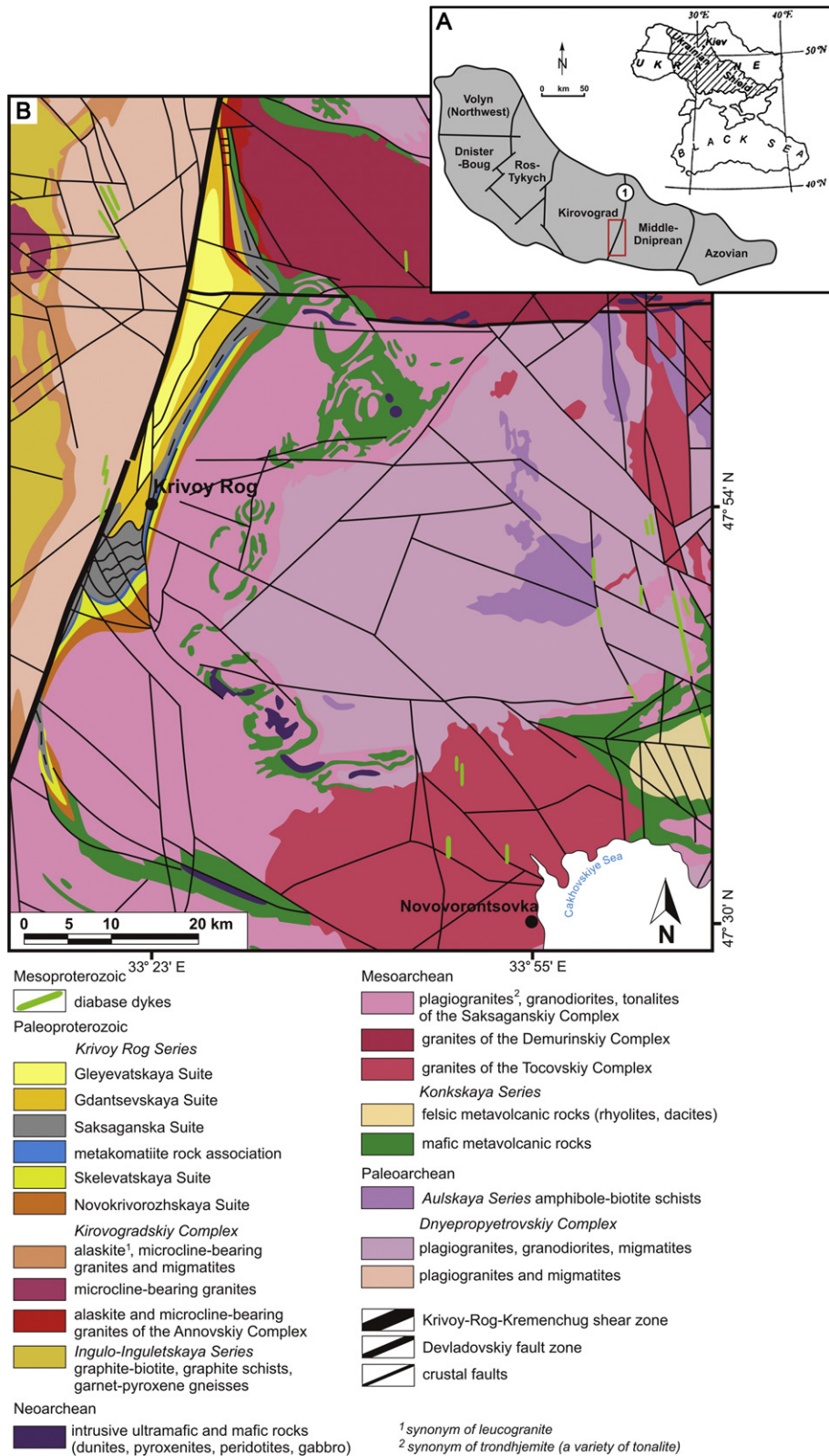


Fig. 1. A—Tectonic provinces of the Ukrainian Shield, 1-Krivoy Rog–Kremenchug megashear (after Bobrov et al., 2002); B—regional geological sketch of crystalline basement of the Ukrainian Shield, Krivoy Rog region (modified, after Paranko et al., 1992).

et al., 2002) (Fig. 2a, b). The Saksaganskiy tectonic block (Fig. 2c), situated in the center of the KRB, is crosscut by the Saksaganskiy thrust zone, which extends its entire length (40 km) (Paranko et al., 1992; Paranko and Butyrin, 2004; Khudur, 2006). The inner structure of the

thrust zone is imbricated and consists of thrust slices, which link with each other in a fan-like manner (Khudur, 2006). The thrust surface dips westward and the dip angle decreases with the depth (Fig. 2a).

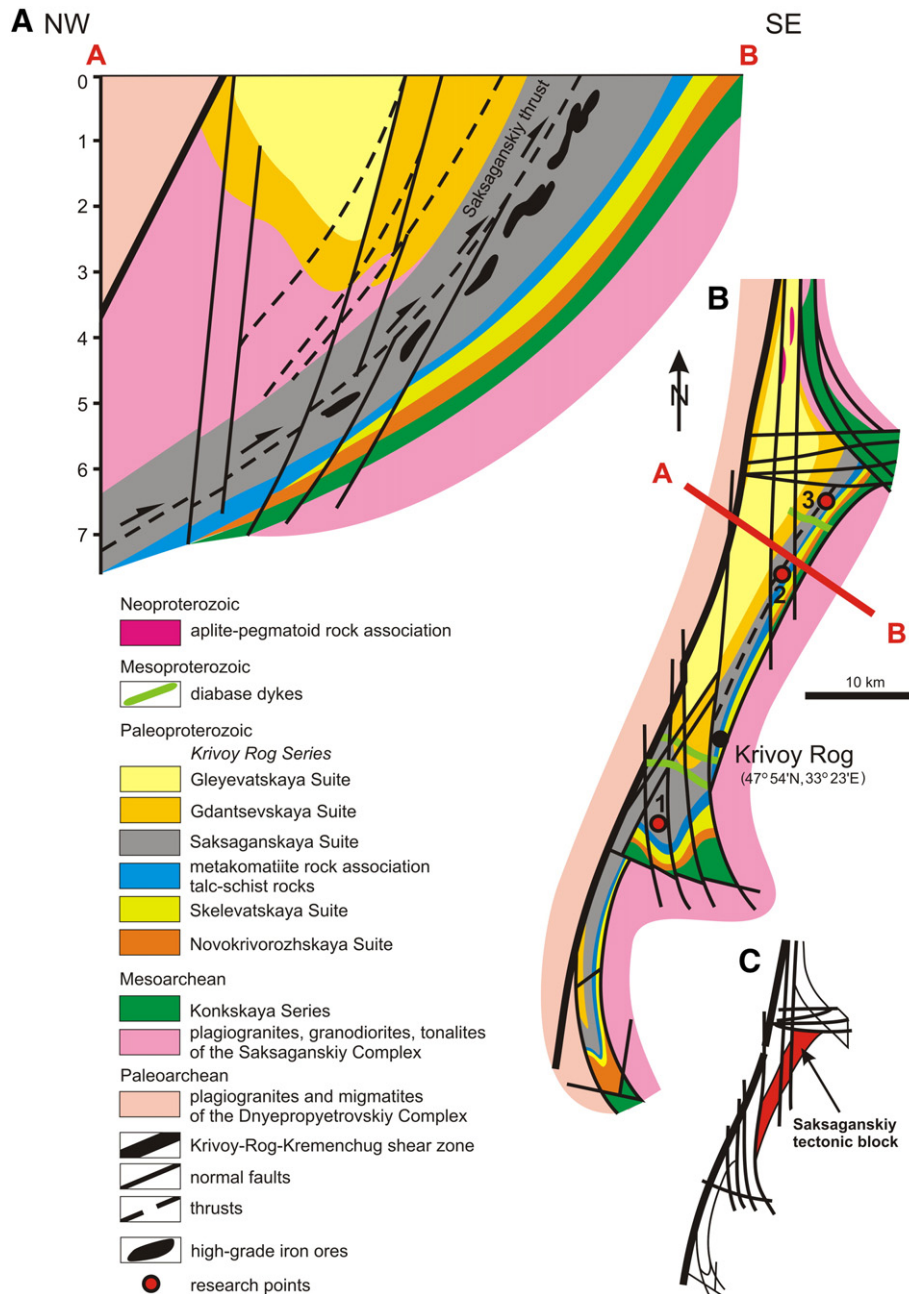


Fig. 2. Geology of the Krivoy Rog Belt (KRB): a—geological cross-section of the central part of the KRB (modified, after Bobrov et al., 2002; Paranko et al., 1992), b—geological map of the KRB (Bobrov et al., 2002), c—tectonic sketch of the KRB (Paranko et al., 1992).

3. Genesis of iron ores

Iron deposits within KRB are confined lithologically to the Saksaganskaya Suite BIF (Belevtsev et al., 1991). The exploited Fe ores are classified based on the Fe content: iron quartzites corresponding to low-grade ores (31–37% Fe), iron-rich quartzites (38–45% Fe) and high-grade ores, which include compacted, massive ores containing ~52–56% of Fe and porous supergene hematite ores comprising up to 60–70% of Fe (Belevtsev et al., 1991). Examples of these ore types are shown in Fig. 4.

3.1. High-grade Fe ores

The Saksaganskiy type, supergene dispersed-hematite-martite high-grade ore (>58% Fe) and epigenetic hypogene, high-grade compacted ores (52–56% Fe) are currently mined underground (e.g. in

the Fruzne mine) in the Saksaganskiy ore field (Saksaganskiy tectonic block). These ores comprise deposits associated with a great variety of structures. In the southern part of the Saksaganskiy block they form steeply dipping bodies occurring in zones of intensive folding and faulting, whereas in the northern part of the block they are associated with fold hinges and flexures (Belevtsev et al., 1991). The high-grade ores form lenses, bed-like or columnar ore bodies within the 5th and 6th iron ore horizons (Belevtsev et al., 1991) and their occurrence is restricted to footwalls of thrust zones controlled by talc-carbonate schists (Fig. 2a) (Paranko, 1993; Shcherbak and Bobrov, 2005).

The hypogene, compacted iron ores from the Saksaganskiy ore field comprise two mineralogical varieties: massive quartz-martite ore (52.5–56.3% Fe) and magnetite ore, 52.01–56.5% Fe, av. 54.5% Fe (Belevtsev et al., 1991). These ores are the precursors to globally recognized martite and dispersed-hematite-martite high-grade Fe ores (>58% Fe according to international standards) composed of

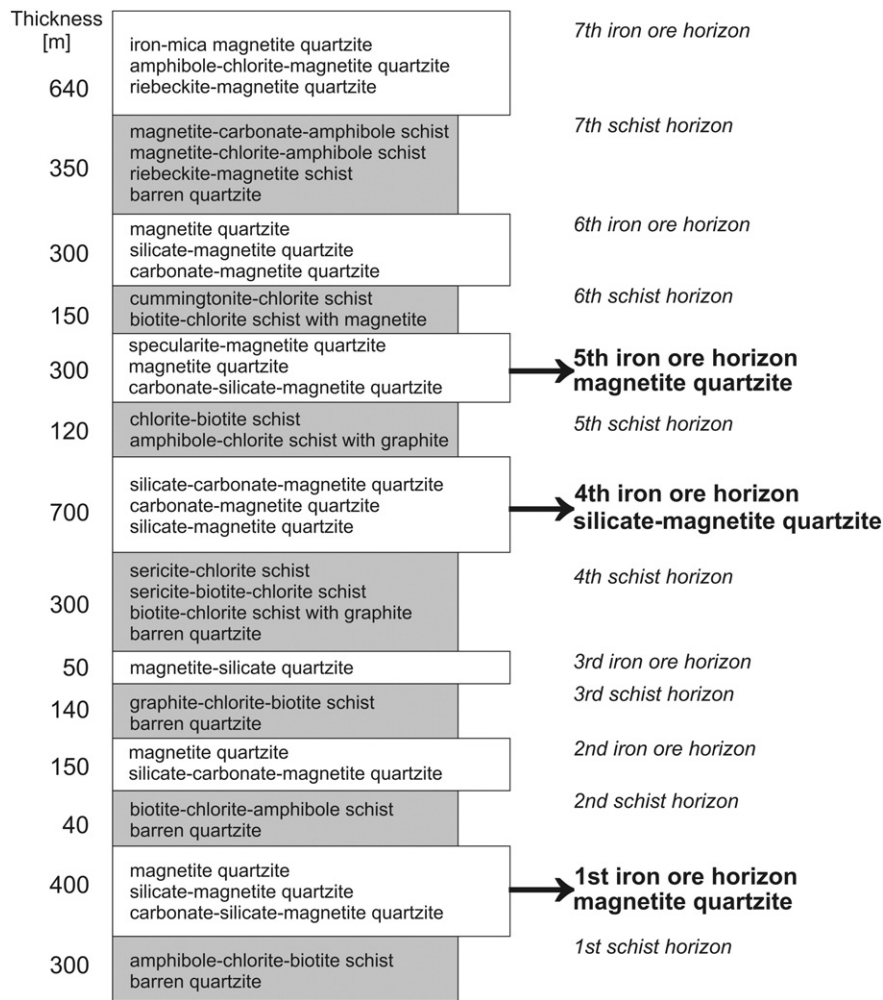


Fig. 3. Generalized lithostratigraphy of the Saksaganskaya Suite (Bobrov et al., 2002), sampled horizons are indicated by arrows.

martite, dispersed hematite and specular hematite (Belevtsev et al., 1991). The quartz–martite ore comprises martite, microplaty hematite and quartz, and it contacts with martite iron quartzites as well as supergene, porous high-grade martite ore, 69.2% Fe (Belevtsev et al., 1991) (Fig. 4H). The hypogene, metamorphic processes are postulated to be responsible for the transformation of martite iron quartzites to the massive quartz–martite ore prior to supergene oxidation (Belevtsev et al., 1991).

3.1.1. Hypogene magnetite high-grade ore

The magnetite ore lacks quartz and is composed of banded magnetite (\pm specular hematite bands) (Belevtsev et al., 1991). Belevtsev et al. (1991) classified it as residual, metamorphic ore, which resulted from gangue subtraction (hypogene metasomatic contraction in local terminology). According to the authors, this formation mechanism involved fluids, which were responsible for removal of gangue minerals e.g. silica from iron quartzites and contemporaneous volume reduction of these rocks (Belevtsev et al., 1991). This genetic model assumes the multistage, hydrothermal alteration of iron quartzites of the 5th and 6th ore horizons by fluids of metamorphic origin, which led to silica migration and generation of quartz veins, lenses and nests close to the high-grade ore bodies (Belevtsev et al., 1991). Therefore the fluids, which percolated through thrust zones controlled by the talc-carbonate schist barriers, played an important role in ore-forming processes (Paranko, 1993; Pieczonka et al., 2011). Upward flow of the hydrothermal fluids, to areas of lower pressures, was accompanied by thrusting (Paranko, 1993). The stressfield that caused

formation of thrusts is not well constrained. According to Yevtekhov and Paranko (1996) the thrusting and hypogene hydrothermal alteration were triggered by the rift basin inversion. This model states that the compressional stress was associated with igneous activity of the adjacent Saksaganskiy plagiogranite massif, which could have been responsible for simultaneous introduction of magmatic–hydrothermal fluids into the system (Khudur, 2006). Evidence of magmatic–hydrothermal fluid flow within the thrust zone that would support this hypothesis is yet to be shown conclusively. An alternative model assumes that the stress was generated by partial subduction of the Middle Dniprean terrane beneath the rigid Kirovogradskiy terrane (Reshetnyak, 1993).

According to the current genetic model the hypogene high-grade ores (52–56% Fe) formed during retrograde metamorphism at temperatures of 195–385 °C, and were subsequently oxidized to supergene hematite high-grade ores (60–70% Fe) during infiltration of descending meteoric waters at temperatures of 115–195 °C (Belevtsev et al., 1991; Kalinichenko, 1992).

3.2. Low-grade Fe ores

The low-grade iron ore comprises the 4th iron ore horizon, which reaches maximum thickness in the southern part of the KRB, where it is exploited in the Yugok open-pit, within the Skelevatske–Magnetitove deposit (Bobrov et al., 2002). The thickness of the 4th iron ore horizon in this deposit decreases from 250–400 m in the northern part to 180–225 m in the southern part (Bobrov et al., 2002). The central part

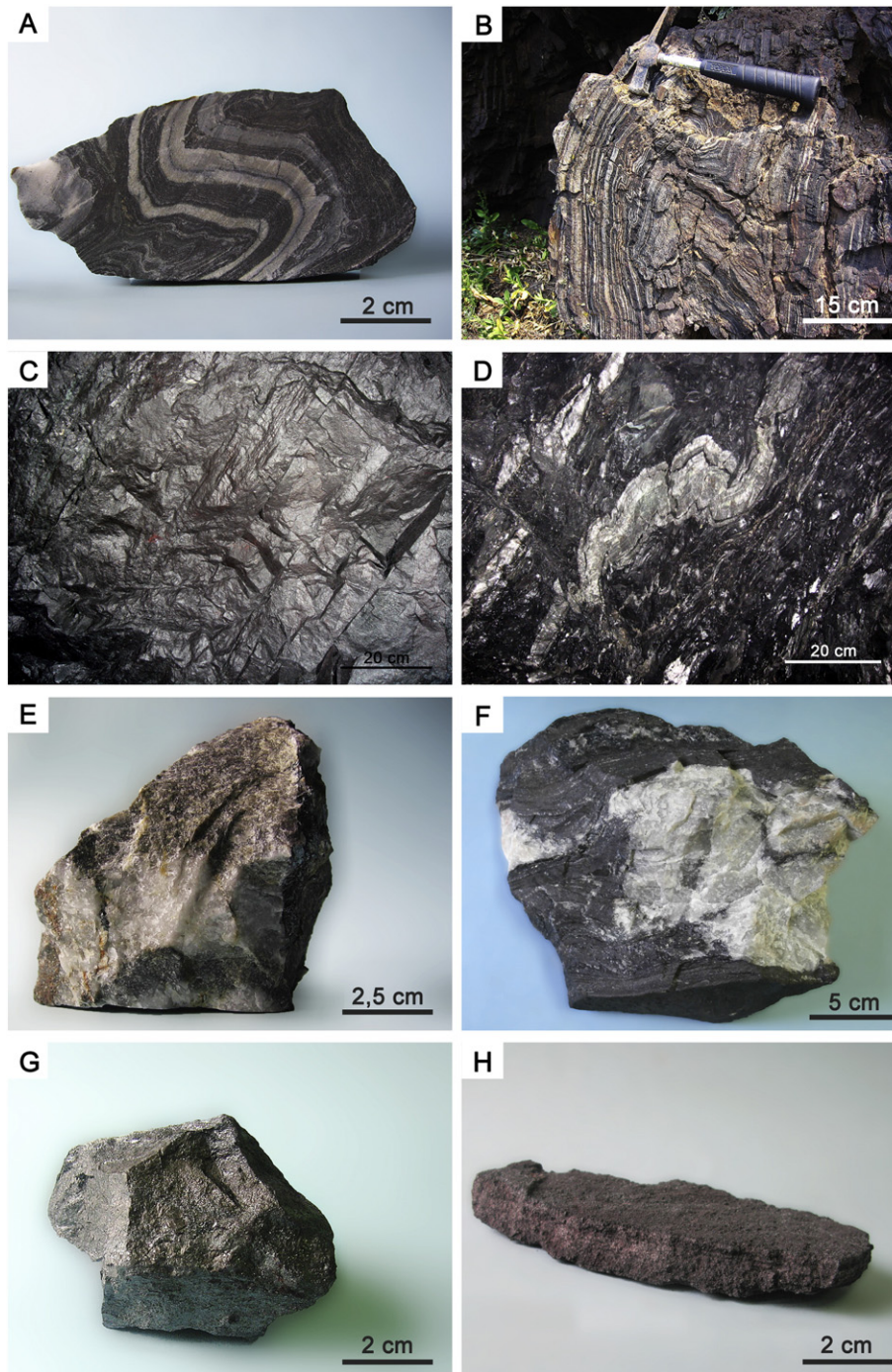


Fig. 4. Iron ore types. A—iron-quartzite, low-grade iron ore, Yugok open-pit, Skelevatske–Magnetitove deposit; B—folded iron-quartzite, MOPR natural outcrop; C—adit wall within high-grade massive, magnetite ore body, exploitation front, 5th iron ore horizon, Frunze underground mine; D—adit wall within the 4th schist horizon (schists with graphite) adjacent to the high-grade ore body, Frunze underground mine; E—quartz vein crosscutting low-grade iron ore, Yugok open-pit, Skelevatske–Magnetitove deposit; F—iron-rich quartzite, Frunze underground mine; G—high-grade massive, magnetite ore, Frunze underground mine; H—porous, martite ore, Frunze underground mine.

is composed of hematite–magnetite quartzites, which are replaced by magnetite, carbonate–magnetite, chlorite–carbonate–magnetite and magnetite–amphibole–chlorite–siderite quartzites towards the margins (Paranko and Mikhnikskaya, 1991; Bobrov et al., 2002). The iron-bearing rocks are isoclinally folded and crosscut by faults. The vertical offset along the main sub-longitudinal Yekaterininskiy fault varies between 20 and 230 m (Bobrov et al., 2002). The oxidation zone (from 3 up to 370 m thick) of the deposit is enriched in martite and limonite (Bobrov et al., 2002). Four varieties of iron quartzites (unaltered by weathering) are exploited in the Skelevatske–Magnetitove deposit: magnetite dominant quartzites (18–32% Fe),

hematite–magnetite quartzites (18–34% Fe), silicate–carbonate–magnetite quartzites (18–23% Fe) and silicate quartzites (18–26% Fe) (Pieczonka et al., 2011). The average Fe content in the deposit is 35.4% (Semenenko, 1978; Bobrov et al., 2002).

4. Sampling

Sampling was carried out within the Saksaganskaya Suite, in the southern and the central parts of the KRB (Fig. 2b).

Observations in Yugok open-pit, located in the Skelevatske–Magnetitove deposit (Fig. 2b, research point 1) were focused on the

low-grade iron ores. Samples of these ores (silicate–magnetite quartzites) and quartz veins (vein 1 and vein 2, samples Ink and K1, respectively) hosted by them were collected from the 4th ore horizon (Fig. 4). Due to safety reasons, sampling was limited to the crushed material underneath the exploitation wall.

A sample of a quartz vein (sample QZ) within iron-rich quartzites (magnetite quartzites) was collected from the wall of the adit, in the Frunze underground mine at the depth of 1135 m, from the 1st ore horizon (Fig. 2b, research point 2). The Frunze mine is located in the Saksaganskiy tectonic block. The sample comes from the ore horizon that is directly in contact with the talc schist horizon and it represents a quartz vein parallel to the dip of the iron-rich quartzites.

High-grade Fe ores were sampled in the Frunze underground mine (Fig. 2b, research point 2, Fig. 4). The high-grade, magnetite ore samples (MGF1 and MGF6) come from the exploitation front of the 5th iron ore horizon (depth of 1135 m). The porous magnetite ore (sample MRF1) was collected from the 1st ore horizon (depth of 1065 m).

Samples of quartz (QBM8, QBM9, QBM811, QBM12) were collected within the Saksaganskiy thrust zone (Fig. 2b, research point 3) developed within the 5th ore horizon (Balka Severnaya Krasnaya natural outcrop), which is comprised of iron quartzites hosting high-grade iron ores. The high-grade ores occur about 100–150 m beneath the quartz sampling site and are associated with folded structures and boudinage close to the thrust zone. The sampling site is located in the footwall of the Saksaganskiy thrust, close to the outcropping mylonites. The samples represent quartz veins and tectonic breccias from a highly silicified zone, which resulted from multiple hydrothermal silica removal and deposition during thrusting.

5. Research methodology

The research included microthermometry and Raman spectroscopy of individual fluid inclusions as well as a bulk method, baro-acoustic decrepitation.

5.1. Microthermometry

Microthermometry of fluid inclusions from quartz veins hosted by low-grade iron ores was conducted in the Fluid Inclusion Laboratory at the University of Leoben in Austria. Fluid inclusions were studied in doubly polished thick sections of approximate thickness between 150 and 170 μm . After detailed petrography studies, heating-freezing experiments were conducted on classified fluid inclusions hosted by quartz. Microthermometry was carried out using a Linkam MDS 600 stage mounted on an Olympus BX 60 optical microscope. Calibration of the Linkam stage was performed using synthetic fluid inclusion standards (pure H_2O , CO_2 – H_2O mixtures) for the melting temperatures of CO_2 at -56.6°C , of H_2O at 0.0°C and the critical homogenization temperature of H_2O at 374.0°C . The reproducibility is $\pm 0.1^\circ\text{C}$ between -60 and $+100^\circ\text{C}$ and $\pm 0.3^\circ\text{C}$ at higher temperatures. Microthermometry data include homogenization temperatures of CO_2 phases, i.e. $T_{\text{h}}(\text{LV} \rightarrow \text{L})$, and clathrate melting temperatures, i.e. $T_{\text{m}}(\text{cla})$ in the presence of one and two CO_2 phases. Microthermometric analyses of fluid inclusions hosted by quartz from the iron-rich quartzites and quartz samples from the thrust zone were made at the Department of Geological Sciences, Stockholm University (Sweden), with a Linkam THM 600 stage mounted on a Nikon microscope utilizing a $40\times$ long working-distance objective. The thermocouple readings were calibrated by means of SynFlinc synthetic fluid inclusions and well-defined natural inclusions in Alpine quartz; melting of pure CO_2 (-56.6°C), melting of water ice (0.0°C), critical homogenization of CO_2 (31.1°C) and critical homogenization of water (374.1°C). The reproducibility is $\pm 0.1^\circ\text{C}$ for temperatures below $+40^\circ\text{C}$ and $\pm 0.5^\circ\text{C}$ for temperatures above $+40^\circ\text{C}$. Digital images were controlled and captured using a Leica EC3 color camera connected to the microscope and Leica LAZ EZ v-2.0.0 computer software. Microthermometry data include total

homogenization temperatures of aqueous fluid inclusions, i.e. $T_{\text{h}}(\text{total})$, melting temperatures of ice, i.e. $T_{\text{m}}(\text{ice})$, clathrate melting temperatures, i.e. $T_{\text{m}}(\text{cla})$ in the presence of one and two CO_2 phases, homogenization temperatures of CO_2 phases, i.e. $T_{\text{h}}(\text{LV} \rightarrow \text{L})$ and melting temperatures of CO_2 , i.e. $T_{\text{m}}(\text{CO}_2)$. Total homogenization temperatures were not measured in order to avoid the risk of decrepitation of H_2O – CO_2 -rich fluid inclusions. The microthermometry results were processed in two software packages: FLUIDS and CLATHRATES (Bakker, 1997, 2003) to evaluate fluid properties. Estimation of volumetric properties of the CO_2 – CH_4 – N_2 fluid inclusions required additional information about the amount-of-substance fractions obtained from the Raman spectroscopy. In order to complete the calculation, volume fractions of the carbonic phase in fluid inclusions at room temperature were additionally estimated (Bakker and Diamond, 2006), using the computer program Image J (Abramoff et al., 2004). Computed bulk compositions and molar volumes were used to calculate isochores in the chosen range of 200 – 700°C , applying equations of state according to Bowers and Helgeson (1983) and Bakker (1999). A ternary compositional diagram was plotted using GCDkit 3.00 (Janousek et al., 2011), whereas histograms of the microthermometric data, were plotted using STATISTICA 10 (StatSoft Inc.).

5.2. Raman spectroscopy

Raman spectroscopy of individual fluid inclusions was essential for confirmation of their compositions and recognition of the solid phase observed in fluid inclusions. The analyses of quartz-hosted fluid inclusions from veins within the low-grade iron ores, were made with a Jobin Yvon LABRAM confocal-Raman spectrometer equipped with a frequency-doubled Nd–YAG green laser (100 mW , 532.2 nm) at the University of Leoben in Austria. The instrument has a spectral resolution of about 1.5 cm^{-1} . The Raman spectroscopy data conversion was made using LabSpec software. Analyses of quartz-hosted fluid inclusions from vein within the iron-rich quartzites and the thrust zone, were performed at Stockholm University, Sweden, using a laser Raman confocal spectrometer (Horiba instrument LabRAM HR 800) equipped with a multichannel air cooled CCD detector. An Ar-ion laser ($\lambda = 514\text{ nm}$) was used as the excitation source with an output power at the sample of 8 mW . The instrument was integrated with an Olympus microscope and the laser beam was focused to a spot of $1\text{ }\mu\text{m}$ with a $100\times$ objective. The instrument was calibrated by repeated use of a neon lamp and the Raman line of a silicon wafer (520.7 cm^{-1}). Instrument control and data acquisition was made with LabSpec 5 software. The crystallization temperatures of graphite were calculated according to Beyssac et al. (2002) using the peaks of the Raman spectra.

5.3. Baro-acoustic decrepitation

Baro-acoustic decrepitation analyses of ore minerals (magnetite bands from the low-grade iron ore, massive high-grade magnetite ore and porous magnetite ore) were conducted at the laboratory of Burlinson Geochemical Services in Darwin, Australia. This method was used to determine formation temperatures of opaque minerals from a large number of fluid inclusions. Prior to analyses the rock material was crushed and sieved into a fine fraction of 200 – $420\text{ }\mu\text{m}$ (80 – 40 mesh). The prepared samples were analyzed with the BGS model 105 decrepitor (see details <http://www.appliedminex.com/decrep/general/model105.htm>). Separated samples of ore minerals were heated at constant rate, while fluid inclusion bursts were simultaneously recorded digitally (Burlinson, 1988, 2008). The decrepitor was calibrated for quality control of the results using standard samples. Unusual samples were analyzed twice and the background levels were checked by re-analyzing material, which had been analyzed before. Decrepigrams were plotted using GnuPlot, version 4.6 (<http://www.gnuplot.info/>). The ore formation temperature was estimated based on

the “onset temperature” (temperature at the toe of the peak), which marks the start of massive decrepitation of fluid inclusions.

6. Fluid inclusion petrography, microthermometry and Raman spectroscopy

6.1. Low-grade iron ore

The low-grade iron ore (silicate–magnetite quartzites), hosts veins 1 and 2, which are composed of coarse to medium grained quartz with minor amounts of carbonates (2% of vein volume). Vein 2 also comprises hematite inclusions and chlorite. The contact between the banded ore and the vein is visible only in vein 1 and it is comprised of fine grained quartz zone, which appears to be transitional in character (Fig. 5A). Vein 1 is oriented perpendicular to the ore layering, whereas vein 2 obliquely crosscuts the banding at a relatively low angle.

Fluid inclusions, observed in vein 1 and vein 2, are primarily grouped into trails or clouds. In general, the trails show a discrete character, usually intersect many crystals or terminate within a single crystal and sometimes crosscut each other (Fig. 5B). The veins also contain decrepitation clusters (Fig. 5C), which are manifested by corrugated black holes representing former inclusions that had undergone decrepitation, leaving surrounding, dispersed satellite inclusions, i.e. a dense cloud of fluid inclusions (Fig. 5D). Fluid inclusion assemblages (FIAs) of unknown origin were also observed and they could not be determined as primary or secondary according to the textural definitions. Fluid inclusions hosted by vein 1 and vein 2 were classified into four types.

6.1.1. Type I

The pseudo-secondary and/or secondary, one-phase (L or V) CO₂-rich fluid inclusions occur in trails and frequently exhibit perfectly negative crystal shapes (Fig. 6A, B). Their sizes are variable and range between 1 and 20 μm.

6.1.2. Type II

The aqueous, two-phase (L + V) fluid inclusions (Fig. 6C) occur very locally within veins and their distribution patterns are impossible to distinguish. They show oval or cylindrical shapes and sizes between 5 and 15 μm.

6.1.3. Type III

Type III comprises pseudo-secondary and/or secondary, two-phase (L + L) aqueous-carbonic (Fig. 6D), three-phase (L + L + V) aqueous-carbonic, three-phase (L + L + S) or (L + V + S) aqueous-carbonic with a solid phase (Fig. 6E, F, G) and four-phase (L + L + V + S) aqueous-carbonic fluid inclusions with a solid phase (Fig. 6H). These fluid inclusions are organized in straight or slightly curved trails and co-exist in single trails despite a different number of phases. Therefore they were approximated by the H₂O–CO₂–NaCl system, locally including an accidentally trapped solid phase. The fluid inclusion data are included in Appendices A, F and G.

Fluid inclusion sizes vary between 12 and 115 μm and regular shapes (cubical, negative crystal shaped, spherical) prevail. The CO₂ volume fraction— $\varphi(\text{CO}_2)$ of fluid inclusions ranges between 0.07 and 0.68 (mode value: 0.19) and it is somewhat consistent within single trails, however it may vary greatly if different trails are compared. The accidentally trapped solid phase, enclosed within several fluid inclusions, is engulfed within single inclusions (Fig. 6E, F) or crosscuts inclusion walls (Fig. 5G). Variably sized minerals show elongated euhedral forms (Fig. 6E, G) or spherical shapes (Fig. 6F) and in some cases they occupy as much as 80% of the fluid inclusion volume (Fig. 6F). Under an optical microscope the crystals are strongly birefringent in cross-polarized light (Fig. 6F) and were identified by three characteristic Raman spectrum peaks (660.04 cm⁻¹, 1047.4 cm⁻¹, 1270.06 cm⁻¹) to be a nahcolite (NaHCO₃).

The homogenization temperatures of CO₂— $T_h(\text{CO}_2)$ vary between –10.4 and +30.9 °C (Fig. 7A), whereas melting temperatures of clathrate— $T_m(\text{cla})$ range between +6.0 and +8.6 °C (Fig. 7B). In all measured inclusions CO₂ homogenized to the liquid phase. $T_h(\text{CO}_2)$ of fluid inclusions hosted by vein 1 exceeded $T_m(\text{cla})$ (homogenization after

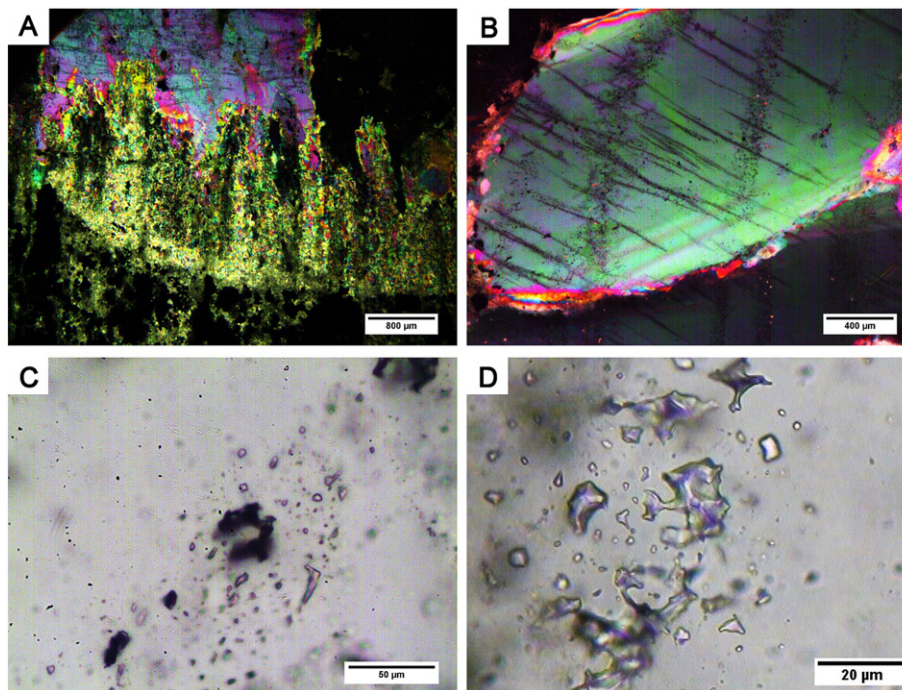


Fig. 5. Fluid inclusion petrography, quartz vein 1 and vein 2, low-grade iron ore. A—a contact zone between the ore and vein 1, B—two systems of fluid inclusion trails within an individual quartz crystal, C—a decrepitation cluster, D—an example of dense cloud of irregular carbonic fluid inclusions.

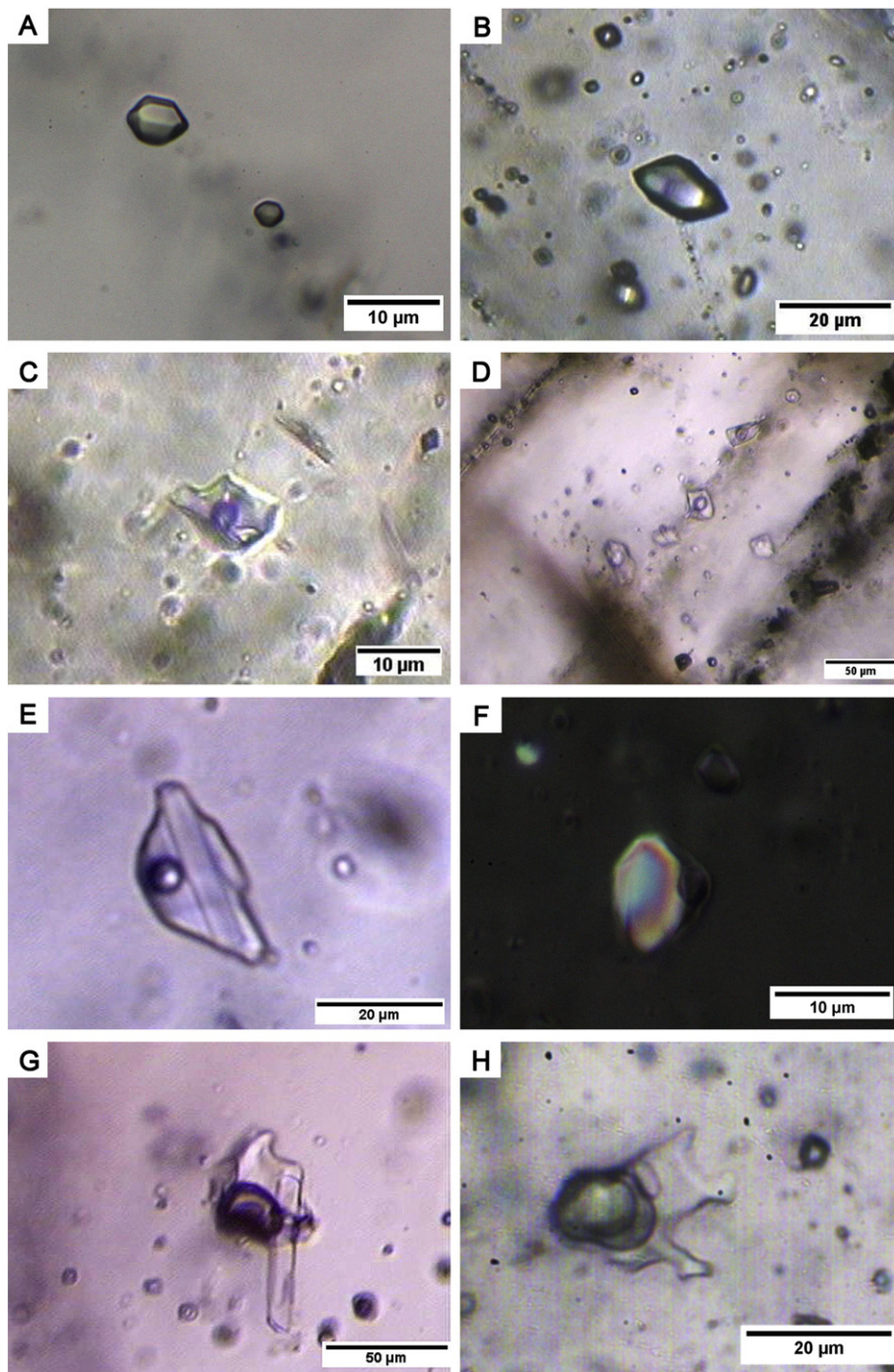


Fig. 6. Fluid inclusion assemblages hosted by quartz vein 1 and vein 2, low-grade iron ore. A—one-phase, liquid, negative crystal shaped, carbonic fluid inclusions (type I), B—one-phase, vapor carbonic fluid inclusion (type I), C—two-phase aqueous fluid inclusion (type II), D—trail of two-phase aqueous-carbonic fluid inclusions (type III), E—a three-phase fluid inclusion (type III) containing an aqueous solution, vapor CO₂ bubble and an engulfed nahcolite crystal, F—a three-phase fluid inclusion (type III) with large birefringent nahcolite occupying almost entire volume of the inclusion (cross-polarized light), G—a three-phase fluid inclusion (type III) comprising an aqueous solution, vapor CO₂ bubble and a nahcolite crystal crosscutting the fluid inclusion wall, H—a four-phase fluid inclusion (type III) containing an aqueous solution, vapor CO₂ surrounded by liquid CO₂ (dark bubbles) and a small nahcolite crystal.

clathrate melting) or were lower than $T_m(\text{cla})$ implying homogenization in the metastable absence of clathrate (Fig. 7A). On the contrary, all fluid inclusions from vein 2 homogenized in the Q_2 conditions (coexistence of the four phases: aqueous liquid, CO₂ vapor, CO₂ liquid, clathrate). CO₂-clathrate melting temperatures below 10 °C in the presence of CO₂ liquid and vapor (i. e. Q_2 melting) indicate the presence of salt in the aqueous phase. It was assumed that the presence of the nahcolite in fluid inclusions had no impact on the measurements due to the petrographical evidence indicating accidental trapping (Fig. 6G) and the random distribution of fluid inclusions with nahcolite on the

histogram suggests a lack of relationship between their $T_h(\text{CO}_2)$ and the presence of this crystal (Fig. 7A). Densities of the CO₂ phase range between 0.52 and 0.99 g/cm³, whereas the total densities of fluid inclusions vary between 0.95 and 0.98 g/cm³. The $x(\text{CO}_2)$ values range between 0.03 and 0.36 with a mode value of 0.10. The salinity of the aqueous phase is low and ranges between 2.46 and 7.21 mass% NaCl equiv.

6.1.4. Type IV

Late, two-phase (L + V) aqueous and three-phase (L + L + V) aqueous-carbonic fluid inclusions are flat and large usually exceeding

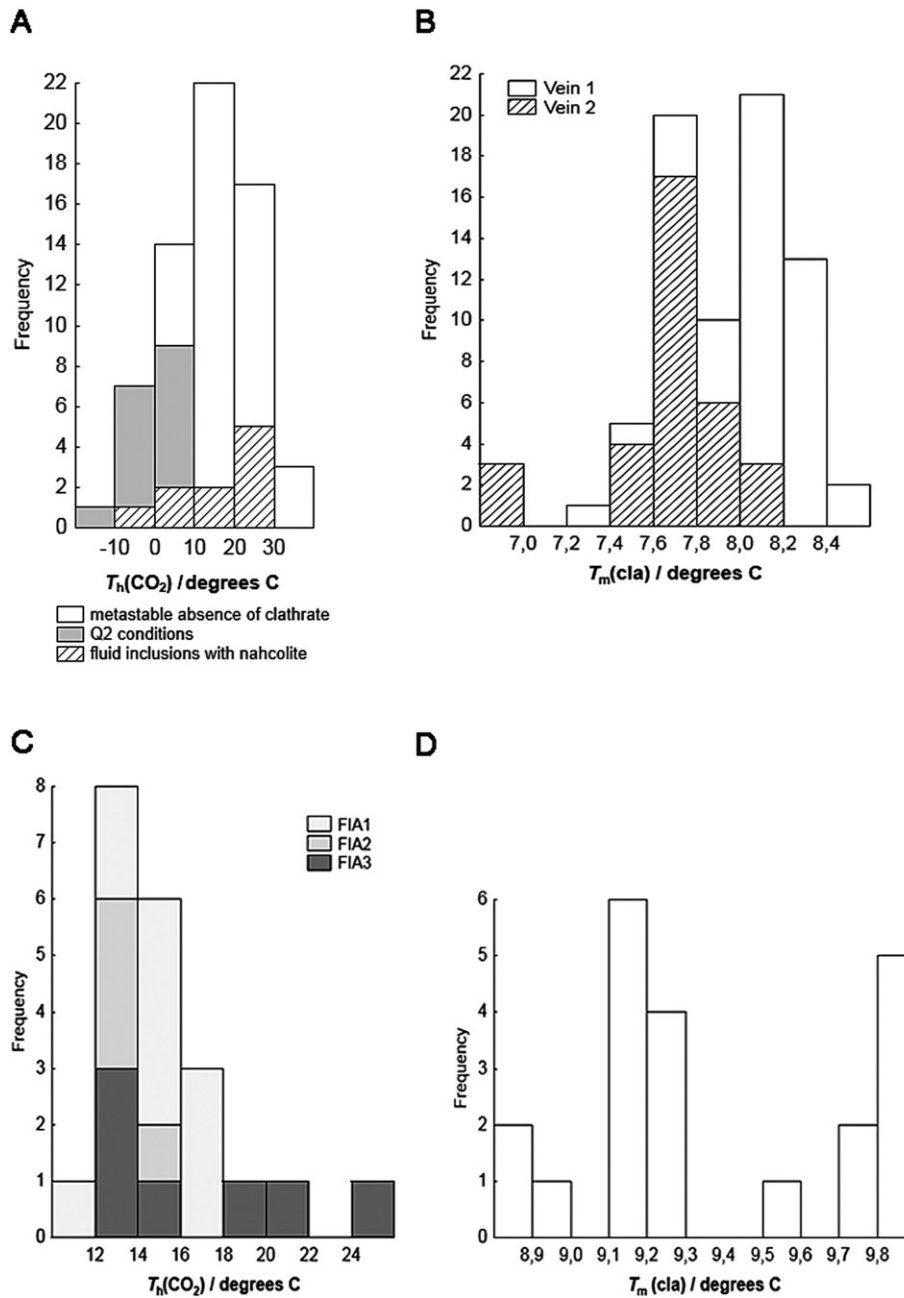


Fig. 7. Histograms illustrating microthermometry results for aqueous-carbonic fluid inclusions in quartz veins from the low-grade iron ore and iron-rich quartzites. A— $T_h(\text{CO}_2)$ of carbonic phases within type III fluid inclusions hosted by quartz vein 1 and vein 2, low-grade iron ore; B— $T_m(\text{cla})$ of type III fluid inclusions hosted by quartz vein 1 and vein 2, low-grade iron ore; C— $T_h(\text{CO}_2)$ of type A fluid inclusions hosted by quartz vein within iron-rich quartzites; D— $T_m(\text{cla})$ of fluid inclusions (type A) hosted by quartz vein within iron-rich quartzites.

100 μm . Their morphologies are not mature, highly irregular and always exhibit sharp corners.

6.2. Iron-rich quartzite

The quartz vein hosted by iron-rich quartzite (magnetite quartzite) is composed of coarse and medium grained quartz and carbonate crystals. Many quartz-hosted fluid inclusions within the vein are randomly scattered and their high density is manifested by darkened areas within the crystals. It was not possible to interpret the origin and timing of these inclusion assemblages.

6.2.1. Type A

Clear parts of the crystals are crosscut by trails of secondary, aqueous-carbonic fluid inclusions – type A (L + L, L + L + V). The

data from these inclusions are included in [Appendices B, F and G](#). They are regularly shaped (spherical, cubic, cylindrical, negative crystal) with some minor exceptions. The sizes range between 6 and 25 μm and the $\varphi(\text{CO}_2)$ varies from 0.09 up to 0.59 (mode value: 0.20).

$T_h(\text{CO}_2)$ range between 11.4 and 25.9 $^\circ\text{C}$ (Fig. 7C) and the inclusions homogenized to the liquid phase after clathrate melting. $T_m(\text{CO}_2)$ values belong to a narrow interval between -58.2 and -56.6 $^\circ\text{C}$ and mode values close to -56.6 $^\circ\text{C}$ indicate the presence of almost pure CO_2 . Slightly decreased $T_m(\text{cla})$ values, between 8.9 and 9.9 $^\circ\text{C}$ (Fig. 7D), suggest negligible amounts of salts in the aqueous phase (salinity of 0.003–1.98 mass% NaCl equiv.). Total densities vary between 0.91 and 0.99 g/cm^3 , whereas densities of the CO_2 phase vary between 0.70 and 0.85 g/cm^3 . The $x(\text{CO}_2)$ values range between 0.06 and 0.36 with a mode value of 0.10.

6.3. Thrust zone

6.3.1. Quartz vein

The vein is composed of coarse quartz crystals, which are generally elongated in one direction with forms commonly close to euhedral (Fig. 8A). The data from petrography, Raman spectroscopy and microthermometry of quartz-hosted fluid inclusions comprising types 1, 2, 3 and CO₂-rich are included in Appendices C, D, F and G.

6.3.1.1. Type 1. Trails of two-phase (L + V), aqueous fluid inclusions (Fig. 8B) may be pseudo-secondary in origin as they usually are located within single quartz crystals (Fig. 8B). The sizes of predominantly regularly shaped fluid inclusions vary between 5 and 29 μm. Their φ_{vap} ranges between 0.07 and 0.31. The Raman analyses of the inclusions revealed that their gas phase is N₂-rich (Fig. 9) as this component occupies as much as 75–98 mol% of the gas bubble volume. The gas phase also contains traces of CH₄ and rarely CO₂ as shown in the compositional diagram (Fig. 9). Exclusively a graphite rim, covering the gas phase of fluid inclusions was detected. Crystallization temperatures of the graphite were 506 °C and 598 °C. The $T_{\text{h}}(\text{LV} \rightarrow \text{L})$ values range between 239 and 299 °C (Fig. 10A) and indicate densities between 0.93 and 0.88 g/cm³. $T_{\text{m}}(\text{ice})$ values are decreased and range between –11.75 and –8.45 °C (Fig. 10B) corresponding to increased salinities, which vary from 12.22 up to 15.72 mass% NaCl equivalent (Fig. 10C). Five fluid inclusions displayed T_{e} (first melting) between –15 and –24 °C suggesting that the prevailing salt is NaCl.

6.3.1.2. Type 2. Two-phase (L + V), aqueous fluid inclusions of type 2 (Fig. 8C) are isolated, however they occur close to the trails of type 1 fluid inclusions. Their sizes range from 10 up to 17 μm and they are all of cylindrical shape. The φ_{vap} of the inclusions varies between 0.14 and 0.19 and their gas phase is N₂-rich (93 mol%) and it contains CH₄ (7 mol%) likewise fluid inclusions comprising type 1 (Fig. 9). The inclusions homogenized at higher temperatures $T_{\text{h}}(\text{LV} \rightarrow \text{L}) = 304\text{--}370$ °C (Fig. 10A) and show slightly higher salinities (15.22 up to 16.76 mass% NaCl equiv.) compared to type 1 fluid inclusions (Fig. 10C).

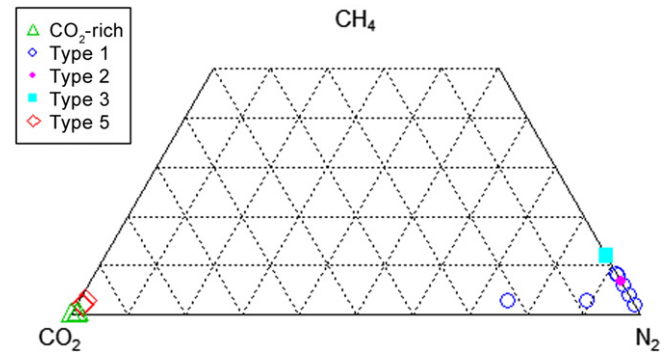


Fig. 9. CO₂–CH₄–N₂ compositional diagram for carbonic fluid inclusions (type 5) from the quartz clasts of the breccia and gas phases of aqueous-rich fluid inclusions (type 1, type 2, type 3, CO₂-rich) hosted by the quartz vein, thrust zone.

6.3.1.3. Type 3. The quartz crystal from the vein contains a cluster of primary two-phase (L + V), aqueous fluid inclusions (Fig. 8D). They are small sized (7–11 μm) and of different but regular shapes: spherical, cylindrical and negative crystal. Their φ_{vap} varies between 0.20 and 0.32 and their gas phase is N₂-rich (88 mol%) and contains higher amounts of CH₄ (12 mol%) compared to the gas phases of type 1 and type 2 inclusions (Fig. 9). The $T_{\text{h}}(\text{LV} \rightarrow \text{L})$ values range from 256 up to 276 °C (Fig. 10A) and are equal to densities between 0.86 and 0.83 g/cm³. Salinities, equal to 6.38 and 7.1 mass% NaCl equiv. (Fig. 10C), are much lower compared to those typical for type 1 or type 2 inclusions.

6.3.1.4. CO₂-rich type. Quartz crystals are filled with consistently dispersed, one-phase, CO₂-rich fluid inclusions of less than 5 μm in size, which may be of a primary origin. They contain 98.8 mol% of CO₂, 1 mol% of N₂ and 0.2 mol% of CH₄ (Fig. 9).

6.3.2. Quartz breccia

The sample of the tectonic breccia comprises angular clasts of quartz and carbonates surrounded by fine to medium grained quartz matrix (Fig. 11A).

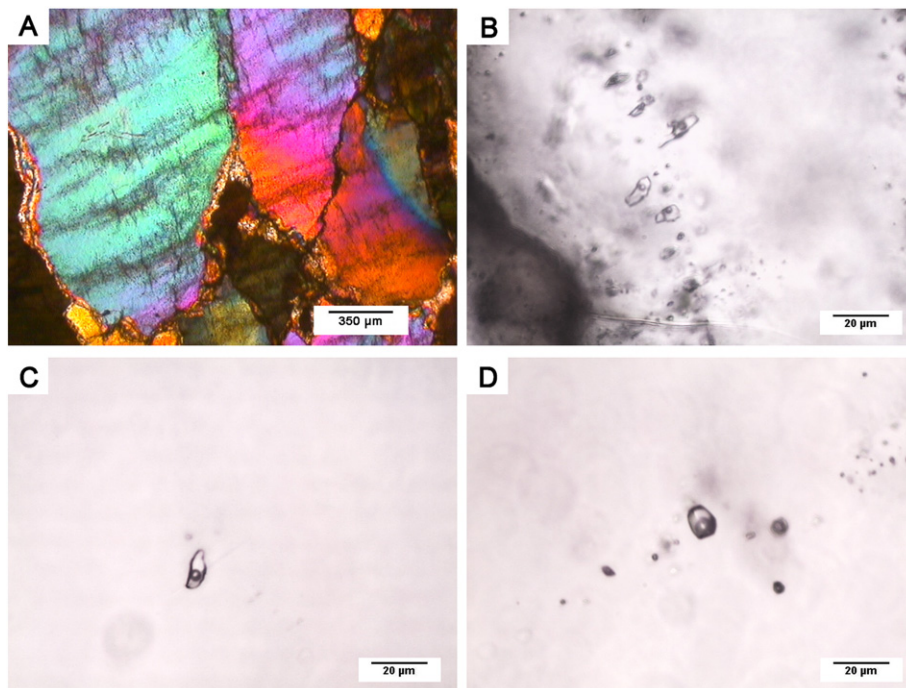


Fig. 8. Fluid inclusion assemblages hosted by the quartz vein from the thrust zone: A—fluid inclusion trails crosscutting quartz crystals, B—a trail of pseudo-secondary or secondary fluid inclusions (type 1), C—an isolated fluid inclusion (type 2), D—a primary or pseudo-secondary fluid inclusion (type 3).

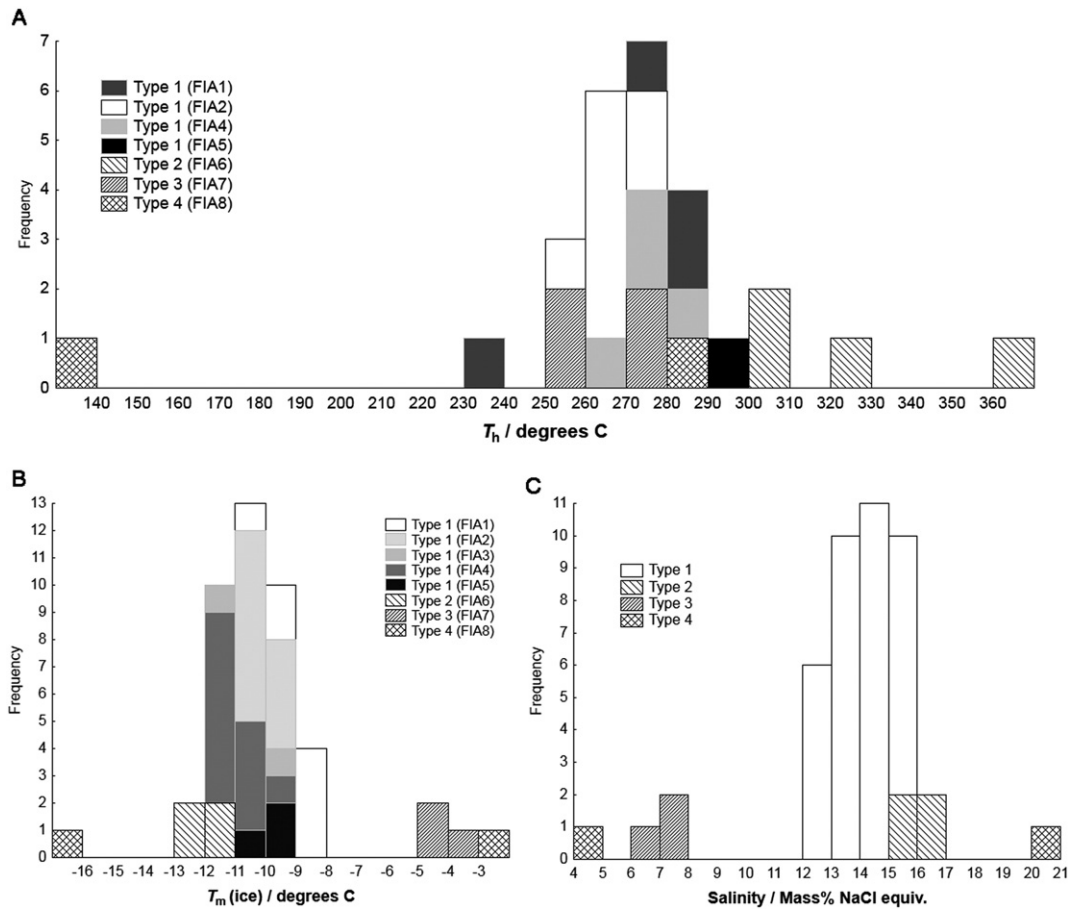


Fig. 10. Histograms illustrating microthermometry results for aqueous fluid inclusions hosted by quartz from the thrust zone: A— T_h (total) in respect of types and FIAs; B— T_m (ice) in respect of types and FIAs; C—salinity in respect of types. Type 1—pseudo- or secondary fluid inclusions, type 2—isolated fluid inclusions, type 3—primary or pseudo-secondary fluid inclusions, and hosted by the matrix of the breccia: Type 4—primary fluid inclusions.

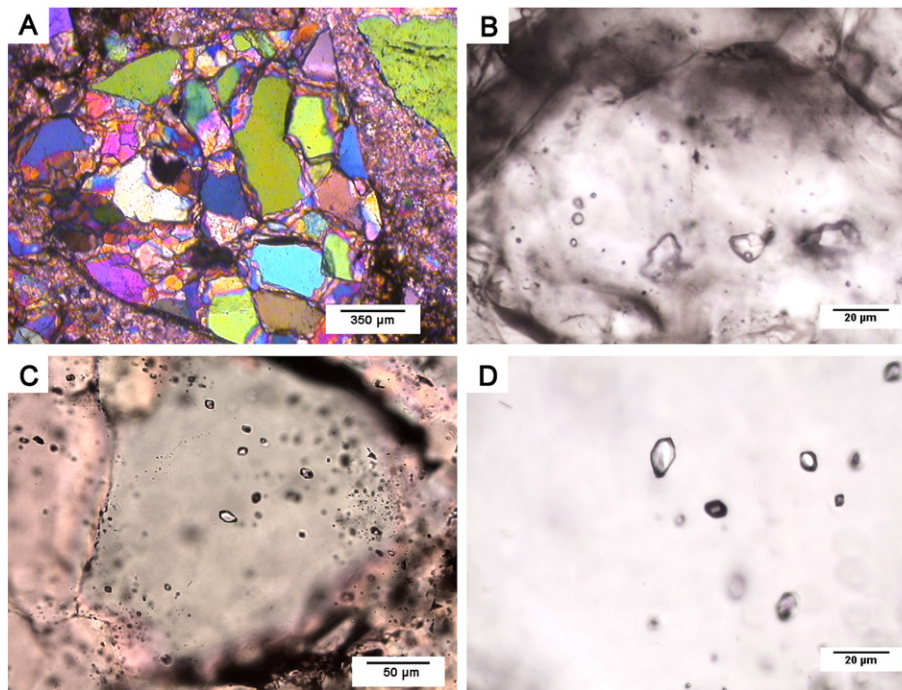


Fig. 11. Fluid inclusion assemblages from the thrust zone. A—a quartz breccia (cross-polarized light), B—coexistence of 3 fluid inclusions in the center of a single quartz crystal from the breccia matrix (from the left: two-phase aqueous—type 4, three-phase aqueous with a solid phase—type 4, one-phase carbonic), C—one-phase, carbonic fluid inclusions (type 5) in a single breccia clast, D—one-phase, carbonic fluid inclusions (type 5) in a center of the breccia clast.

6.3.2.1. *Type 4.* The quartz crystal of the matrix contains three different primary fluid inclusions coexisting with each other: two-phase (L + V) aqueous – type 4 (18 μm, $\varphi_{vap} = 0.19$), three-phase aqueous (L + V + S) with a solid phase – type 4 (12 μm) and one-phase carbonic (L) (20 μm) (Fig. 11B). The two-phase, aqueous fluid inclusion (type 4) is irregular in shape and homogenized at $T_h(LV \rightarrow L) = 283$ °C. The density of the fluid within inclusion is 0.94 g/cm³, whereas the $T_m(ice) = -16.85$ °C (Fig. 10B) indicates a high salinity of 20.11 mass% NaCl equiv. (Fig. 10C). The angular, three-phase fluid inclusion (type 4), containing a cubic crystal, partly homogenized at $T_h(LVS \rightarrow LS) = +130$ °C. Its gas phase is covered by a graphite rim ($T_{cryst} = 525$ °C), whereas the salinity of the aqueous solution (4.87 mass% NaCl equiv.) is significantly lower compared to the salinity of coexisting two-phase inclusion. This fact together with lack of response during Raman analysis suggests that the visible cubic phase (Fig. 11B) is a daughter crystal of halite, which indicates the true salinity of the fluid inclusion of nearly 35 mass% NaCl equiv.

6.3.2.2. *Type 5.* Quartz clasts contain primary, one-phase (L) fluid inclusions, which are rarely accompanied by several solid inclusions of hematite. The fluid inclusions (7–24 μm) tend to be spherical, cylindrical, cubic or negative crystal shaped (Fig. 11C, D). They were frozen to nucleate a gas bubble at low temperatures and subsequently heated to acquire $T_h(LV \rightarrow L)$ in a range between –46.5 and –35.4 °C corresponding to densities between 1.072 and 1.03 g/cm³ (Appendices E, F, G). Decreased $T_m(CO_2)$ values, varying between –60.3 and –61.9 °C (Fig. 12), indicate the presence of CH₄ and N₂ (Fig. 9). According to the Raman data the average CH₄/N₂ ratio is 3:1, therefore these fluid inclusions belong to the CO₂–CH₄–N₂ system.

7. Baro-acoustic decrepitation

The analyses of two samples of magnetite from the low-grade iron ore show one major peak, typical for magnetite (Fig. 13). The magnitudes differ significantly, which is probably caused by variations in the abundance or sizes of fluid inclusions. The onset temperatures, generalized for both veins, are around 530 °C.

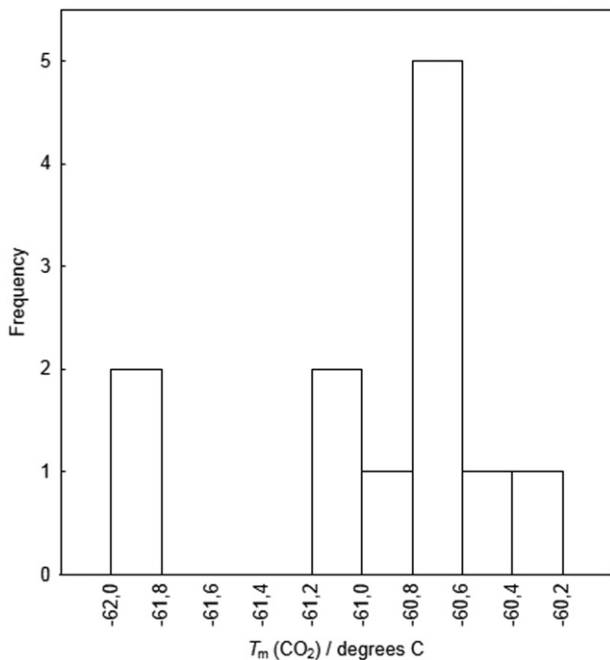


Fig. 12. $T_m(CO_2)$ of one-phase, carbonic fluid inclusions (type 5) hosted by quartz breccia clasts, thrust zone.

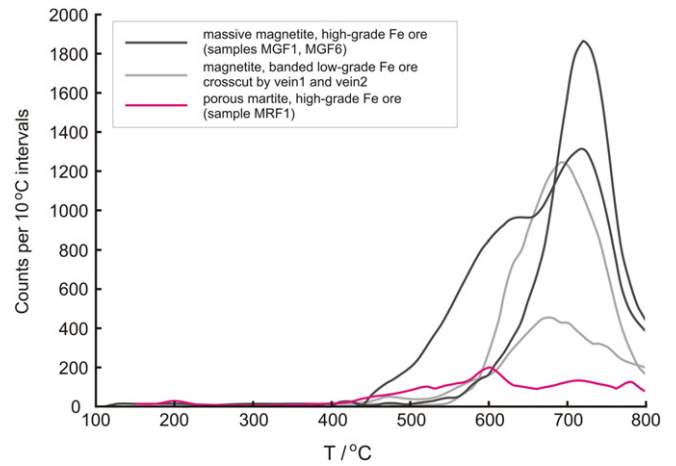


Fig. 13. The results of the baro-acoustic decrepitation of fluid inclusions hosted by ore minerals comprising low-grade iron ore (banded magnetite) from Yugok open pit and high-grade massive magnetite ore and porous martite ore from Frunze underground mine.

Both samples from the high-grade massive, magnetite ore, MGF1 and MGF6 come from the same sampling site but from different specimens. Sample MGF6 comprises almost pure magnetite, whereas sample MGF1 contains thin specular hematite layers alternating with magnetite layers. This slightly differing mineralogy probably affected the decrepitation curves, which show different numbers of peaks as well as the peak intensities (Fig. 13). The main intensity peaks remain in almost the same temperature interval and the onset temperatures range from 430 up to 500 °C.

The porous martite ore (sample MRF1) shows much lower decrepitation intensity compared to the magnetite ores indicating a low abundance of fluid inclusions. Very low decrepitation is observed at the onset temperature around 400 °C (Fig. 13).

All decrepitation curves lack a low-temperature peak around 200 °C, indicating an absence of CO₂-rich fluid inclusions.

8. Interpretation

8.1. Fluid types

Based on the fluid inclusion petrography and compositional data from microthermometry and Raman spectroscopy, quartz veins within the low-grade Fe ore host fluid inclusions representing four types of fluids: carbonic, early and late aqueous and low salinity H₂O–CO₂(±N₂–CH₄)–NaCl(±NaHCO₃). The quartz vein from iron-rich quartzites preserved one distinguishable type of fluid: H₂O–CO₂(±N₂–CH₄) ± NaCl. Five types of fluids could be distinguished within the thrust zone: CO₂–CH₄–N₂(±C), CO₂(±N₂–CH₄), low salinity H₂O–N₂–CH₄–NaCl, moderate salinity H₂O–N₂–CH₄–NaCl(±CO₂, ±C) and high salinity H₂O–NaCl(±C). Magnetite from the low-grade iron ore and massive, high-grade ore contains fluid inclusions, which represent most probably two different aqueous fluids, however their exact compositions remain unknown. A summary table of fluid inclusion types is included in Appendix H.

Fluid compositions differ depending on the associated iron ore type. Fluids from the thrust zone, which are strictly related to the hypogene high-grade ore mineralization (Paranko, 1993; Pieczonka et al., 2011), are clearly distinct from fluids that circulated within the low-grade iron ore (iron quartzites) and iron-rich quartzites. The highest salinities are characteristic of fluids related to the thrust zone, whereas very low fluid salinities are typical of iron-rich quartzites and the low-grade iron ore. Fluids from the thrust zone are much more enriched in methane compared to those from the low-grade and iron-rich quartzites.

8.2. Trapping mechanisms

8.2.1. Iron quartzites (veins)

Secondary, aqueous-carbonic fluid inclusions hosted by quartz veins within the low-grade iron ore (type III) and iron-rich quartzites (type A) are similar. They show moderate variability of $\varphi(\text{CO}_2)$, which may be also expressed as calculated $x(\text{CO}_2)$. The $x(\text{CO}_2)$ variation (Fig. 14) may suggest changes produced by re-equilibration processes during uplift and decompression of the rocks (Bodnar, 2003). However, there is a lack of significant relationship between $x(\text{CO}_2)$ and $T_h(\text{CO}_2)$ values (Fig. 14). The trend remains constant apart from a few outliers and this eliminates the possibility of compositional re-equilibration (i.e. leakage of an aqueous solution from aqueous-carbonic fluid inclusions) as the density of the CO_2 phase does not decrease with increasing size of the CO_2 bubble. If the loss of the aqueous solution through microfractures occurred, the CO_2 phase should have become enlarged, simultaneously containing lower density fluid (Hollister, 1990). The $x(\text{CO}_2)$ vs. $T_h(\text{CO}_2)$ relationship may also indicate that CO_2 -rich inclusions (type I) were not formed due to the removal of aqueous solution from adjacent aqueous-carbonic fluid inclusions. The spread values of $x(\text{CO}_2)$ may also be considered as a result of heterogeneous trapping as this mechanism is common in natural fluid inclusions and it may produce very different $\text{H}_2\text{O}/\text{CO}_2$ volume ratios due to multiple immiscibility episodes (Roedder, 1984; Diamond, 2003). However, the predominance and bimodal distribution of end-member phase ratios for example, which could be an evidence for immiscible fluid trapping (Bodnar, 2003), was not noticed in aqueous-carbonic fluid inclusions, instead the whole range of middle volume ratios occurs.

The presence of accidentally trapped nahcolite within type III inclusions, hosted by quartz veins from the low-grade iron ore, introduces further uncertainty. The accidental enclosure is clearly shown by uneven distribution in fluid inclusions and variable sizes of crystals, sometimes even exceeding the sizes of the fluid inclusions themselves. This implies that nahcolite could have been selectively trapped during temperature decrease in one of the fluid flow stages.

If the diversity of $x(\text{CO}_2)$ values of fluid inclusions hosted by quartz veins from the low-grade iron ore (type III) and iron-rich quartzites (type A) did not result from compositional re-equilibration or heterogeneous trapping it may be attributed to variation of a fluid source. One of the possibilities is successive trapping of fluids differing in compositions during their intermittent release into the system. The spread of $x(\text{CO}_2)$ values and densities of fluid inclusions could have resulted from fluid entrapment in conditions of oscillating pressure primarily associated with a crack-seal mechanism (Ramsay, 1980). It includes repeating cycles of crack and seal events. While cracking, the fluid-filled crack is

opening with a simultaneous pressure build-up accompanying the fracturing (Ramsay, 1980). In contrast, during a sealing event, higher permeability enables fluid percolation through the crack network and triggers a pressure decrease (Ramsay, 1980). Pressure fluctuations could have been the cause of the density and $x(\text{CO}_2)$ diversity. This assumption may also be supported by the fact that the $\varphi(\text{CO}_2)$ variability occurs between the different trails, but not among fluid inclusions of a single trail. Therefore, the fluid inclusions most probably resulted from homogeneous trapping of fluids of different densities, which were introduced repetitively into the system in geological time.

In summary, the mechanism of fluid entrapment was primarily homogenous, excluding the episodes responsible for the formation of the nahcolite crystals related to fluid inclusions hosted by quartz veins from the low-grade iron ores. Fluids of various densities were incrementally expelled into the system during multiple fluid flow episodes in metamorphic stage.

8.2.2. Thrust zone

The interpretation of trapping mechanisms of aqueous fluids from the thrust zone is complex due to the tectonic setting associated with high strains and pressures, which may generate possible immiscibility episodes and post-entrapment modifications of fluid inclusions.

All fluid inclusion assemblages (type 1–4 inclusions) group into tight clusters as illustrated in the bivariate plot showing relationship between $T_h(\text{total})$ and $T_m(\text{Ice})$ values (Fig. 15). This diagram may be interpreted in terms of evolution of the aqueous fluids. The earliest were primary fluid inclusions of type 3. The coexistence of these low salinity fluid inclusions and CO_2 -rich fluid inclusions within one quartz crystal may be interpreted as the result of immiscibility of the aqueous-carbonic fluid. However the change of fluid composition during the crystal growth is more probable as the type 3 inclusions occur in the center of the crystal, whereas the CO_2 -rich inclusions are located close to the crystal margins. CO_2 -rich fluid inclusions, situated close to the type 3 as well as type 1 inclusions, are assumed to be primary in origin and were also trapped during the earliest stages. Primary carbonic fluid inclusions from the breccia clasts (type 5) are also associated with these stages.

During the following stage the secondary fluid inclusions (type 1, type 2) were trapped. Moderately variable T_h values of aqueous fluid inclusions of type 1 may be attributed to re-equilibration or variable P–T–X conditions of trapping (Goldstein and Reynolds, 1994). The diagram illustrating a relationship between $T_h(\text{total})$ and φ_{vap} (Fig. 16) indicates re-equilibration as a possible reason of a moderate range of T_h values. The positive trend suggests that the density depends on the size of a gas bubble. The φ_{vap} increase and simultaneous decrease of density

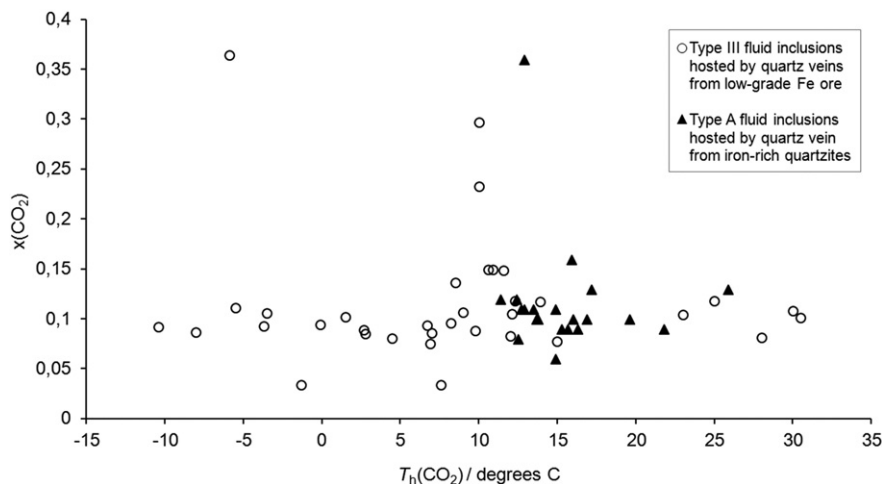


Fig. 14. Relationship between homogenization temperatures of CO_2 – $T_h(\text{CO}_2)$ and amount of CO_2 fraction– $x(\text{CO}_2)$, aqueous-carbonic fluid inclusions hosted by quartz veins from low-grade Fe ore (type III) and iron-rich quartzites (type A).

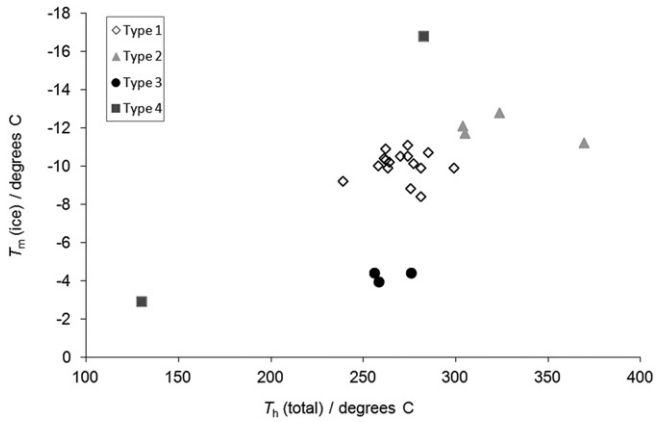


Fig. 15. Bivariate plot showing clusters of data for aqueous, two-phase fluid inclusions hosted by quartz from the thrust zone; type 1—secondary fluid inclusions, type 2—isolated fluid inclusions, type 3—primary fluid inclusions, type 4—primary fluid inclusions from the quartz matrix of the breccias.

was most probably caused by leakage of an aqueous solution from fluid inclusions. It is highly probable that the secondary fluid inclusions (type 1) re-equilibrated in higher P–T conditions to form a fluid trapped as the type 2 inclusions. In this case the leakage and refilling of the type 1 inclusions had occurred and led to formation of fluid inclusions of lower densities but of slightly higher salinities (type 2) (Fig. 15). This fact indirectly proves an input of fluids of higher salinities into the system.

The highest salinity, primary fluids (type 4) were introduced in the latest stage. The aqueous fluid inclusions may be the high salinity end-members of the unmixed magmatic fluids as they were accompanied by carbonic inclusions, which might have additionally favored immiscibility processes (Robb, 2005). However, these fluids might also have been delivered from different sources.

In summary, according to petrographical evidence and microthermometric data, the evolution of aqueous fluids from the thrust zone (types 1–4) was initiated by introduction of low salinity fluids, followed by moderately saline fluids and subsequent input of fluids of high salinities. The trapping mechanisms are ambiguous due to re-equilibration processes and possible immiscibility episodes.

8.3. Trapping P–T conditions

8.3.1. Iron quartzites (veins)

Estimation of the minimum P–T conditions of trapping of aqueous-carbonic fluid inclusions hosted by quartz veins within the low-grade iron ore (type III) and iron-rich quartzite (type A) required plotting of isochores (Fig. 17) as the $T_h(\text{total})$ were not measured. The isochores

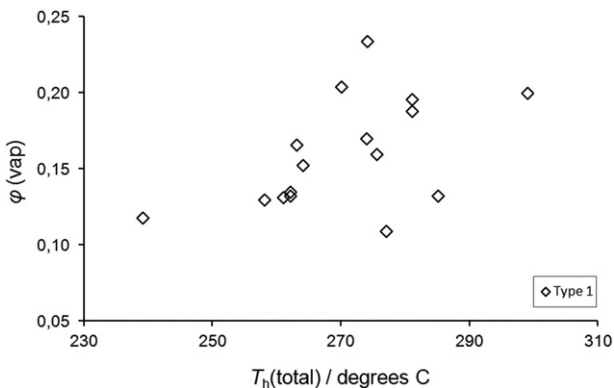


Fig. 16. Diagram showing relationship between total homogenization temperatures and volume fraction of a vapor for secondary, aqueous fluid inclusions (type 1).

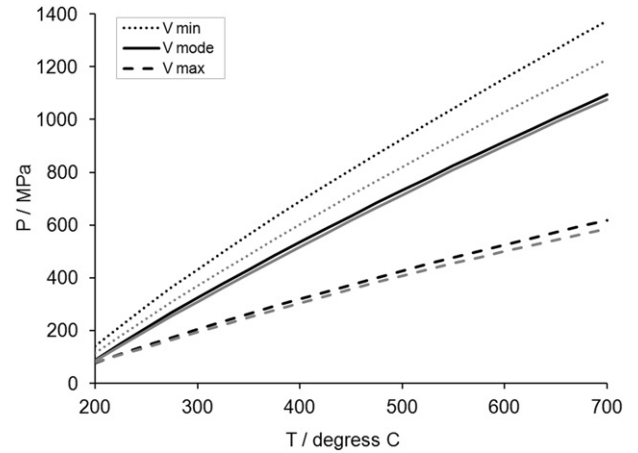


Fig. 17. The P–T diagram of isochores plotted for fluid inclusions of V_{min} , V_{mode} and V_{max} , hosted by quartz veins from low-grade iron ore-type III (gray) and quartz vein from the iron-rich quartzites-type A (black).

were constructed based on the recalculated microthermometric data for fluid inclusions of minimum, maximum and mode volumes (Fig. 17). The majority of the fluid inclusions followed the P–T pathway, which is shown by the isochore plotted for the modal volume. The diagram clearly illustrates that the majority of fluid inclusions of type III as well as type A followed a very similar P–T path and were trapped in a similar range of P–T conditions, despite the fact that they are hosted by veins within different iron ores collected from various localities.

The assumptions that the $\text{H}_2\text{O}-\text{CO}_2$ fluids, trapped as type III and type A inclusions, were initially homogenous and contained on average 10 mol% of CO_2 as indicated by $x(\text{CO}_2)$ mode values (Fig. 14), were essential for constraining the P–T range. Intersection between the isochores and the isopleth for 10 mol% CO_2 , which separates the liquid–liquid immiscibility region for the $\text{H}_2\text{O}-\text{CO}_2$ system (Töðheide and Franck, 1963), provided the minimum temperature– T_t and minimum pressure– P_t of trapping. Fluid inclusions of type III were trapped at $T_{t \text{ min}} = 231 \text{ }^\circ\text{C}$ and $P_{t \text{ min}} = 130 \text{ MPa}$ (vein 1: $T_{t \text{ min}} = 231 \text{ }^\circ\text{C}$, $P_{t \text{ min}} = 154 \text{ MPa}$; vein 2: $T_{t \text{ min}} = 246 \text{ }^\circ\text{C}$, $P_{t \text{ min}} = 130 \text{ MPa}$), whereas type A inclusions were trapped at $T_{t \text{ min}} = 219 \text{ }^\circ\text{C}$ and $P_{t \text{ min}} = 158 \text{ MPa}$. The P–T diagram combined together with isochore charts and facies fields of regional metamorphism clearly indicates that the homogeneous aqueous-carbonic fluids were trapped in conditions tracing the main isochores within the greenschist and amphibolite facies (Fig. 18).

The upper P–T limits of fluid inclusion trapping were in majority constrained by P–T conditions of the regional metamorphism. The maximum T_t of fluid inclusions of type A did not exceed $T_t = 510 \text{ }^\circ\text{C}$, what corresponds to upper temperature limit of regional metamorphism in the Saksagan region. The maximum T_t of type III inclusions corresponds to the upper temperature limit of metamorphism ($T = 600 \text{ }^\circ\text{C}$) in the Skelevatske–Magnetitove deposit. However, the presence of the accidentally trapped nahcolite may be an additional constraint. Fluid inclusions containing this solid phase were formed in conditions not exceeding the melting temperature of the entrapped crystal, which is $270 \text{ }^\circ\text{C}$ (Hoshino et al., 2006).

8.3.2. Thrust zone

The minimum T_t of primary, aqueous fluid inclusions from the thrust zone (type 3, type 4) correspond to the measured $T_h(\text{total})$. According to the petrographical evidence and microthermometry data, the type 3 fluid inclusions were trapped in early stage of quartz vein formation at minimum T_t varying between 256 and $276 \text{ }^\circ\text{C}$. Primary fluid inclusions of type 4, hosted by the breccia matrix, were enclosed in the late stages at higher minimum $T_t = 283 \text{ }^\circ\text{C}$. The secondary, aqueous fluid inclusions (type 1) were formed in the middle stage at uncertain

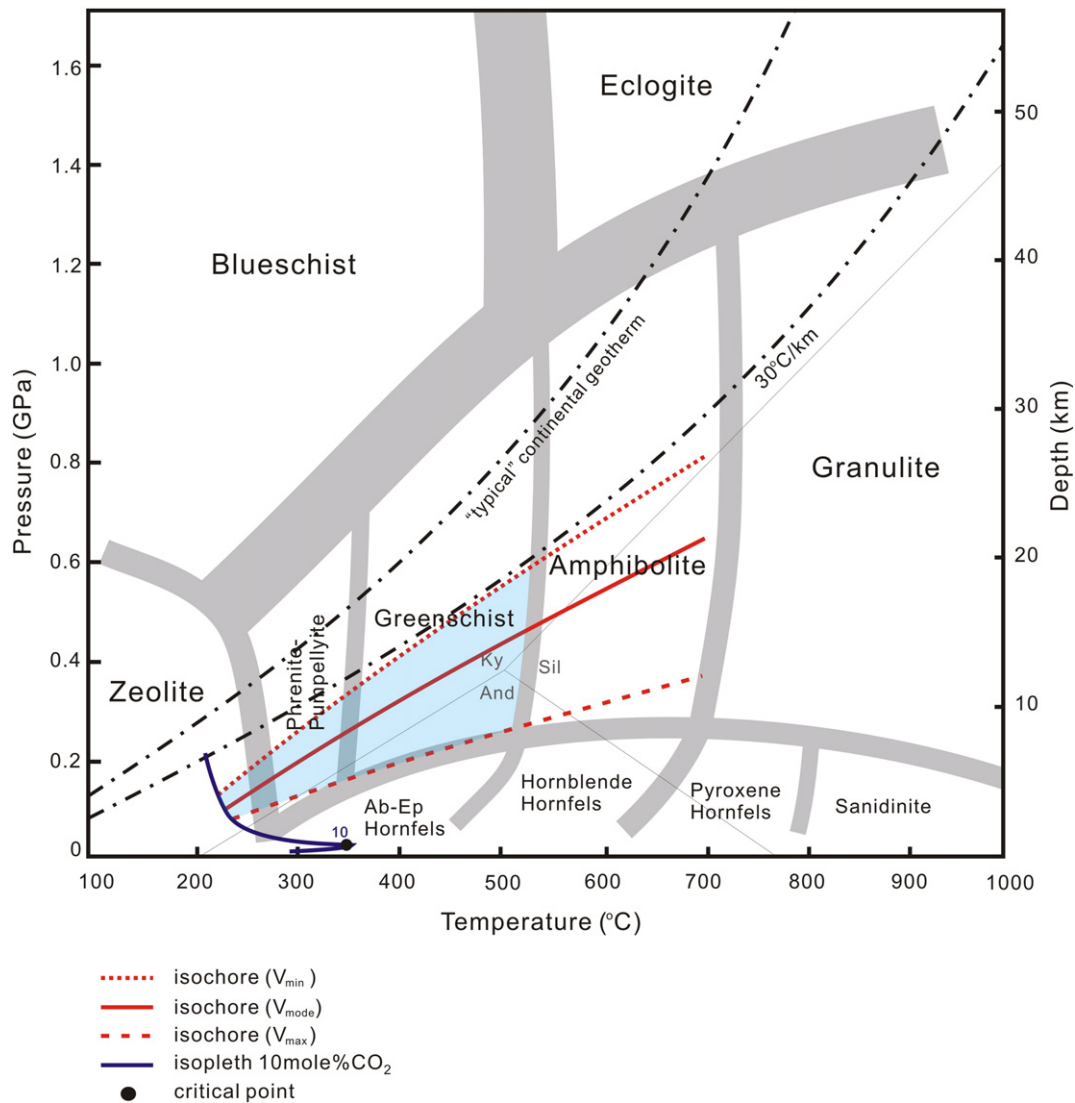


Fig. 18. The P–T diagram showing metamorphic facies from Winter (2001), combined with isochores plotted for the H₂O–CO₂ fluid inclusions hosted by quartz veins from low-grade iron ore (type III) and vein from iron-rich quartzites (type A), and the isopleth for 10 mol% of CO₂. The blue field confines possible range of P–T conditions of the fluid inclusion entrapment.

temperatures as these fluid inclusions underwent compositional re-equilibration and did not preserve the original trapping P–T conditions. Fluid inclusions of type 1 re-equilibrated at temperatures between 239 and 299 °C leading to the formation of type 2 inclusions at higher minimum T_f varying between 304 and 370 °C. The upper T_f limit, which was experienced by fluid inclusions hosted by quartz from the thrust zone, may be confined by the crystallization temperature of graphite, which varies between 506 and 598 °C in type 1 inclusions and in type 4 is equal to 525 °C. Mylonitic and brecciated textures noticed within the thrust zone typically indicate high strain and high pressure environments and therefore precise estimation of pressure limits is problematic.

8.3.3. Low-grade and high-grade Fe ores

The baro-acoustic decrepitation data provided clues to the origin and approximate formation temperatures of magnetite comprising low-grade as well as high-grade iron ores. High peak intensities typical for decrepitation curves of this mineral imply a hydrothermal or metamorphogenic genesis. The approximate formation temperature of magnetite bands from the low-grade iron ore, corresponding to the onset temperature around 530 °C, is higher compared to formation

temperatures of massive magnetite from high-grade iron ore, which vary between 430 and 500 °C. These results suggest that magnetite comprising bands of the low-grade iron ore was formed at higher temperatures compared to magnetite from massive, high-grade iron ore. Most probably the fluid inclusions hosted by magnetite from the low-grade iron ore preserved characteristics from prograde regional metamorphism. The fluid inclusions present in the high-grade magnetite ore most probably preserved the temperatures of metasomatic fluids. Martite, which is a pseudomorph after magnetite, gave a typical low intensity decrepitation response pointing towards a supergene origin, during which the most of the original fluid inclusions were destroyed.

8.4. Fluid sources

The results of the fluid inclusion analyses were combined with the salinity–temperature diagram as illustrated in Fig. 19 (Beane, 1983). According to this diagram the fluid systems of the Krivoy Rog BIF were supplied from different sources: metamorphic, magmatic and meteoric, excluding low-temperature basinal brines.

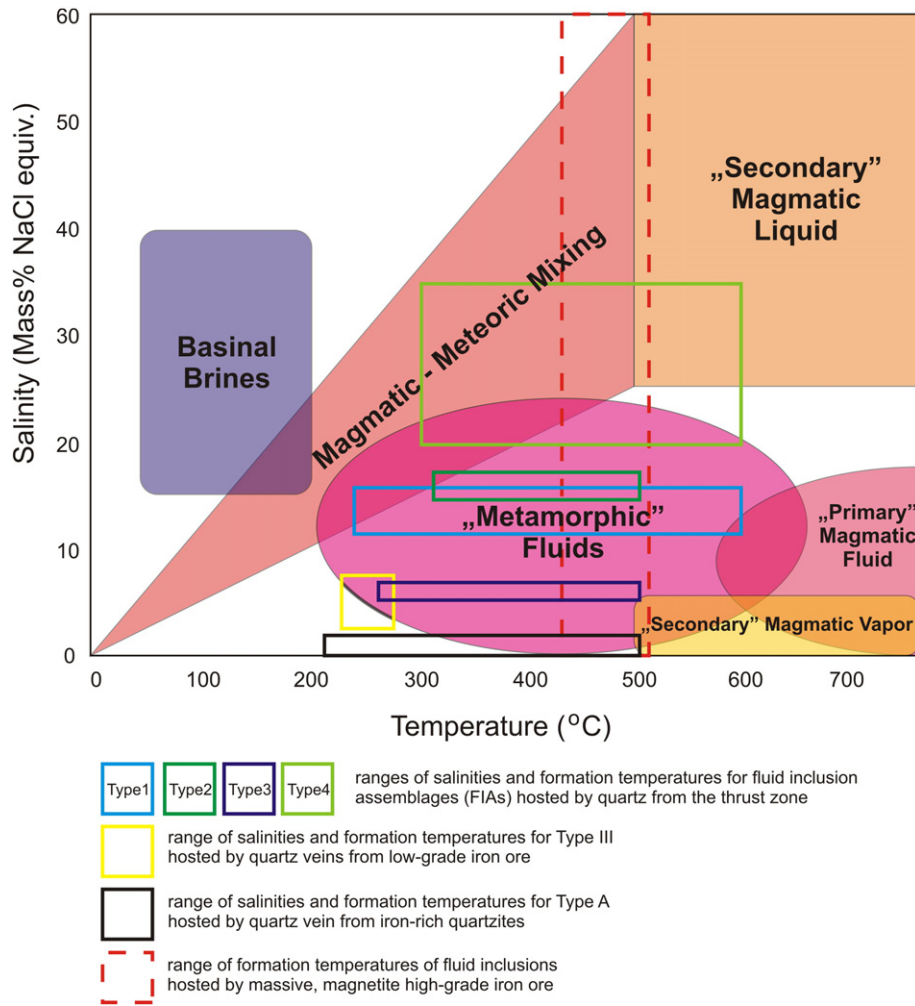


Fig. 19. Ranges of salinities and trapping temperatures of fluid inclusions hosted by quartz veins from the low-grade iron ore, iron-rich quartzites and the thrust zone, combined with approximate temperature–salinity distributions for hydrothermal solutions of different origins (from Beane, 1983).

8.4.1. Iron quartzites

Type III and type A inclusions hosted by quartz veins from the low-grade iron ore and iron-rich quartzite represent metamorphic fluids of low salinities (Fig. 19) trapped on the retrograde path during uplift. The veins are related either to peak-metamorphic or early post-metamorphic conditions, therefore they were able to preserve fluid pulses representative of that environment. However, the early evolution and sources of fluids circulating within the low-grade iron ore are not clear due to the uncertain origin of the nahcolite. This mineral might have originated from Na–K metasomatism or might have been derived from weathering of the alkaline granites supplying the Krivoy Rog basin with a clastic material (Kulik and Korzhnev, 1997). Hoshino et al. (2006) assumed that the nahcolite precipitation resulted from fluid immiscibility (boiling) and the primary fluids responsible for its crystallization contained high amounts of Na^+ and CO_2 , and low quantities of Cl^- .

Varying densities of CO_2 within fluid inclusions, accompanied by admixtures of CH_4 and N_2 in a gas phase, suggest more than one source of fluids and fluid–wall rock interactions. Carbonic-rich fluids interacted probably with schists or other fluids, which led to enrichment in N_2 and CH_4 . The metamorphic veins are hosted by the silicate–magnetite as well as magnetite quartzites, therefore it is highly probable that one of the metamorphic reactions generating CO_2 was decarbonation of iron carbonates resulting in magnetite formation (Belevtsev et al., 1991).

Reactions such as siderite conversion into oxides and silicates that releases CO_2 into the system, are believed to be a very important factor affecting iron ore formations (Perry and Ahmad, 1981). Belykh et al. (2007) indicated similar processes resulting in the formation of metamorphic magnetite for unaltered Proterozoic BIFs of the Kursk Magnetic Anomaly (KMA).

8.4.2. Thrust zone

Aqueous fluids from the thrust zone were divided into 3 groups in terms of salinity: fluids of low, moderate and high salinity (Fig. 19). The fluids of low (type 3 inclusions) and moderate salinities (type 1, type 2 inclusions) are attributed to metamorphic origin, whereas the fluids of the highest salinity (type 4 inclusions) may be the result of mixing of supersaturated magmatic–hydrothermal fluids and metamorphic and/or meteoric fluids (Fig. 19). Type 4 fluid inclusions represent a fluid, which may initially have been formed by immiscibility producing a secondary magmatic liquid and vapor (Fig. 19). These phases subsequently underwent dilution by fluid mixing during circulation through channels within the thrust zone, whereas the vapor end-member was not preserved. The input of the high-salinity fluids might have been associated with activity of the adjacent Saksaganskiy massif, which took place during the late stage of closure of the former rift basin. The crust thickening at that time, led most probably to delamination and upwelling of the asthenosphere, which in turn triggered partial

melting of rocks and subsequent igneous and volcanic activity of the Saksaganskiy massif. The magmatic activity of this massif may also be explained by generation of a mantle plume beneath the Dnyepropetrovskiy terrane, although these hypotheses, both novel for this region, require verification and more research. On the other hand, infiltration of heated basinal brines may also produce fluid inclusions of high salinity (type 4 inclusions). Nevertheless, if the brines were involved, instead of the magmatic–hydrothermal fluids, they required a heat source, e.g. the Saksaganskiy massif, to attain high temperatures (minimum $T_f = 283$ °C). Highly saline, hot brines might have pervasively leached iron from surrounding rocks during upward migration. Fluid inclusions, which trapped ancient meteoric water ($T_h = 115$ – 195 °C), were documented in supergene quartz from the dispersed-hematite–martite, high-grade ores by Kalinichenko (1992). If these temperatures are not true constraints, the possibility of influence of the fluids from the thrust zone described in this paper on the formation of the dispersed-hematite–martite high-grade ores as well, cannot be neglected.

High-grade, magnetite ores were formed in a temperature range (430–500 °C) suggesting that the iron ore upgrade might have been facilitated by fluid immiscibility and mixing (Fig. 19).

The gas phase of aqueous fluid inclusions, representing H_2O – N_2 – CH_4 – $NaCl$ and H_2O – N_2 – CH_4 – $NaCl$ ($\pm CO_2$, $\pm C$) fluids, contains admixtures of N_2 prevailing over CH_4 (types 1, 2, 3). The nitrogen may come from the mantle or may be a result of fluid interaction with graphite schists (Fig. 4D) and decomposition of clay minerals in temperatures around 500 °C (Faure and Mensing, 2005). The latter possibility is supported by crystallization temperatures exceeding 500 °C, which were calculated for graphite found within fluid inclusions (types 1, 4, 5). The graphite might have resulted from a reaction of CO_2 with an aqueous solution or it might have precipitated during heating generated perhaps by late, high-temperature fluids.

The carbonic-rich fluid inclusions (type 5 and CO_2 -rich type) represent fluids derived from at least two different sources. The CO_2 – CH_4 – N_2 ($\pm C$) fluid, preserved as type 5 inclusions, might have been enriched in reduced C during interaction with surrounding rocks, e.g. graphite schists. The fluid evolution suggests a relatively long transport, therefore it might also have been supplied from the deep-seated Krivoy-Rog Kremenchug fault zone. The CO_2 ($\pm N_2$ – CH_4) fluids, represented by CO_2 -rich type inclusions, may be associated with metamorphic decarbonation.

9. Implications for the genetic model

9.1. Metamorphic stage

The earlier, metamorphic stage occurred in all localities and affected all rocks of the Krivoy Rog BIF. In this stage, the low-grade iron ore (iron quartzites) and iron-rich quartzites were formed. The low-grade iron ore was progressively metamorphosed at temperatures around 530 °C as indicated by the decrepitation analysis. During this episode, circulating metamorphic fluids precipitated silica to form quartz veins. According to the fluid inclusion analysis vein formation was determined by fluctuating metamorphic conditions, especially a fluctuating pressure. The minimum P–T conditions for the vein formation were $T_{min} = 219$ – 246 °C and $P_{min} = 130$ – 158 MPa. The metamorphic fluids showed different densities and typically contained CO_2 and low salinity aqueous solution up to 7.21 mass% NaCl equiv. Four kinds of percolating fluids were distinguished within all types of iron quartzites: CO_2 -rich, H_2O , H_2O – CO_2 ($\pm N_2$ – CH_4)– $NaCl$ ($\pm NaHCO_3$) and H_2O – CO_2 ($\pm N_2$ – CH_4)– $NaCl$. The origin of nahcolite ($NaHCO_3$) remains unclear. The fluids were derived from metamorphic reactions, dehydration and decarbonation. Decomposition of Fe-bearing carbonates might have played a significant role in the generation of metamorphic magnetite leading to enrichment of barren quartzites to the low-grade Fe ore and iron-rich quartzites.

9.2. Metasomatic stage

The later, metasomatic stage occurred only within the Saksaganskiy tectonic block and was strictly associated with the Saksaganskiy thrust zone.

9.2.1. High-grade Fe ores (Frunze mine)

The porous, martite high-grade ore was formed by supergene oxidation, which removed fluid inclusions during replacement of magnetite by martite. In contrast, the massive magnetite high-grade ore preserved fluid inclusions, which were trapped at temperatures close to 430–500 °C. These temperatures are close to the upper limit of regional metamorphism in the Saksagan region and suggest that fluid inclusions might have preserved a thermal signature other than metamorphic, however more analyses are required to support this suggestion. The fluid composition was not possible to unravel, but it most likely does not contain CO_2 . It is proposed that the fluid inclusions may comprise a high salinity aqueous solution. The magnetite high-grade ore, most probably, resulted from fluid alteration of magnetite quartzites.

It is anticipated that the Fe ore upgrade to the magnetite high-grade ores might have involved fluids similar, at least to some degree, to those which are described within the Saksaganskiy thrust zone. This assumption is supported by location of these ores within the 5th ore horizon in the footwall of the thrust zone, restriction to the same tectonic block and also to the presence of the talc-schist horizon encountered within the Frunze mine. However, this mine is situated near the boundary, which divides the Saksaganskiy ore field into northern and southern parts based on differentiation between the structure types hosting the iron ore deposits. The processes which generated the structural variability are not well constrained, therefore it is not clear if they were entirely similar for Fe deposits in the Frunze mine as well as beneath the Balka Severnaya Krasnaya outcrop.

9.2.2. Thrust zone

This study reveals and emphasizes the importance of the multiple fluid flow events in the Saksaganskiy thrust zone. According to the compositional and textural features of fluid inclusions three episodes involving different fluids were distinguished within this zone (Fig. 20). These events were contemporaneous with thrusting and brecciation.

Episode I was dominated by introduction of the CO_2 -rich fluids. It involved 3 metamorphic primary fluids of different compositions: CO_2 – CH_4 – N_2 ($\pm C$), CO_2 ($\pm N_2$ – CH_4) and low salinity H_2O – N_2 – CH_4 – $NaCl$ (Fig. 20). The carbonic fluids were probably derived from decomposition of carbonates or/and from deeper sources. Minimum temperatures of the low salinity (6.38–7.1 mass% NaCl equiv.) aqueous fluids were 256–276 °C. Country rocks within the shear zones (e.g. schists) interacted with these fluids supplying them with CH_4 and N_2 . An interaction of the CH_4 -enriched fluids with hematite might have caused its reduction to magnetite.

During episode II the aqueous fluids H_2O – N_2 – CH_4 – $NaCl$ ($\pm CO_2$, $\pm C$) of moderate salinities (15.22–16.76 mass% NaCl equiv.) were expelled into the system (Fig. 20). They were most probably of metamorphic origin and their $T_h = 239$ – 370 °C vary greatly due to re-equilibration. These fluids were N_2 -rich and the origin of this component is ambiguous as it might have been derived from the mantle or from country rocks.

Episode III was associated with high salinity (20.11–35.0 mass% NaCl equiv.) H_2O – $NaCl$ ($\pm C$) fluids of $T_{min} = 283$ °C (Fig. 20). The fluid inclusion analysis suggests that these fluids resulted from mixing of metamorphic and secondary magmatic fluids or introduction of heated basinal brines.

The aqueous fluids show an increase in salinity from early to late episodes (Fig. 20). This trend supports multiple, incremental input of high salinity fluids into the thrust zone through time. Metamorphic low-salinity, aqueous fluids might have periodically mixed with hot, high salinity magmatic–hydrothermal fluids or heated basinal brines. The

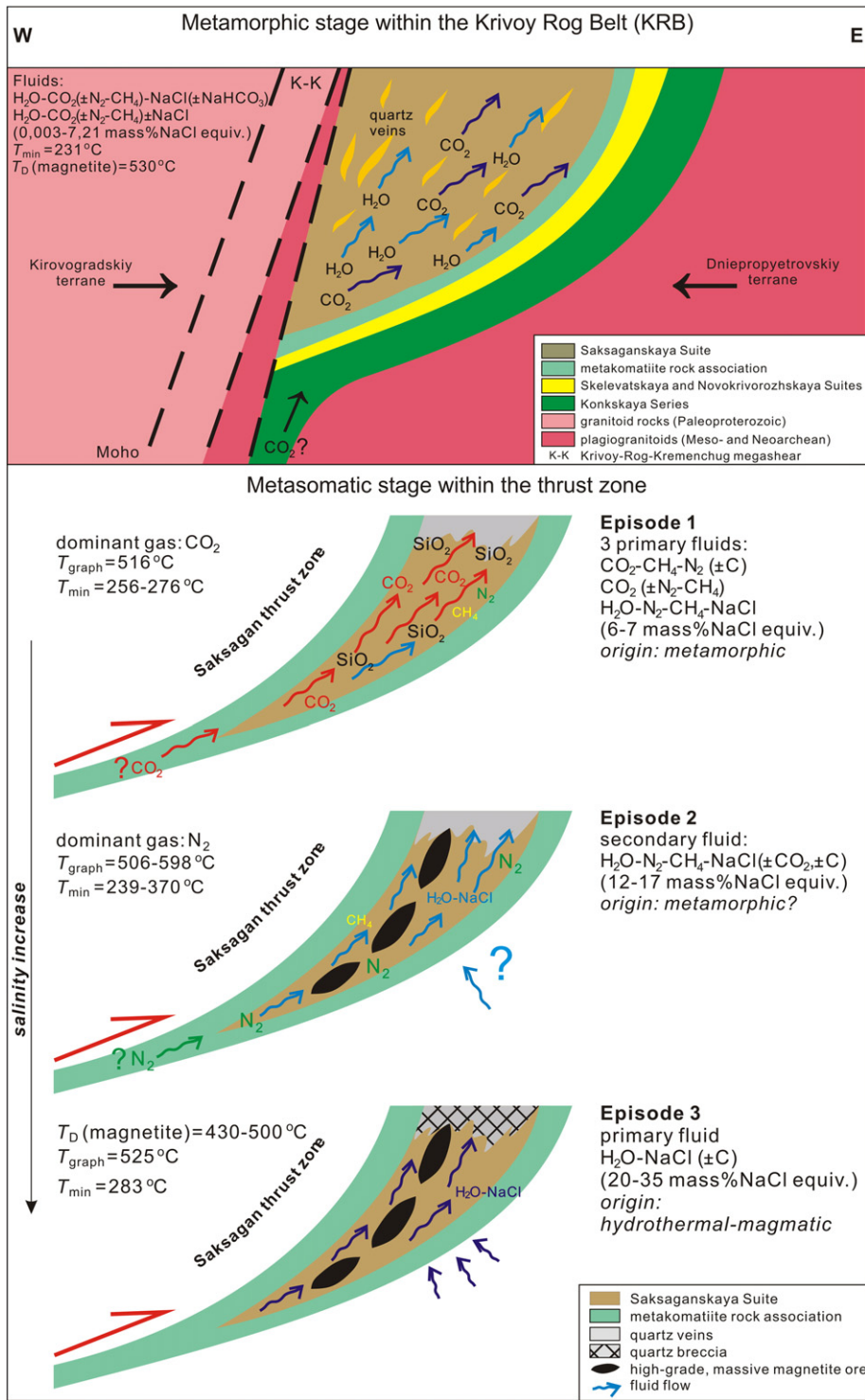


Fig. 20. Schematic illustrations showing metamorphic fluid flow stage within the Krivoy Rog Belt and episodes of multiple fluid flow (metasomatic stage) within thrust zone during the upgrade of iron quartzites (low-grade iron ore and iron-rich quartzites) to massive, high-grade iron ores.

crystallization temperatures of graphite detected in quartz-hosted fluid inclusions exceeded $500^\circ C$. This fact, together with the decrepitation results, may suggest that the iron ore upgrade to high-grade, magnetite ore took place during all episodes at temperatures close to $430-500^\circ C$. The enrichment was facilitated by a complex interaction of BIF with carbonic-rich and low salinity aqueous fluids of metamorphic origin and hot, high salinity fluids, most probably, prior to infiltration of

lower temperature meteoric waters responsible for supergene oxidation. The activity of the adjacent Saksaganskiy igneous body, which initiated thrusting, might have been responsible for introduction of the high salinity magmatic-hydrothermal fluids or heating up the basinal brines. These hot, high salinity fluids might have become enriched in iron due to pervasive alteration of the metavolcanic Konkskaya Series or lower iron quartzite horizons of the Krivoy Rog BIF.

10. Concluding remarks

The fluid inclusion study of Fe ores from the Krivoy Rog district revealed that the history of fluid evolution within the Saksaganskiy ore field is more complex compared to the exploitation area of the Skelevatske–Magnetitove deposit, which is located outside this tectonic unit.

The study indicates the structurally controlled, hot, high salinity fluid flow in the vicinity of the high-grade Fe ore bodies in contrast to areas of the low-grade Fe ore exploitation, where this type of fluid was absent. The low-grade iron ores and iron-rich quartzites were not altered by external fluid influx and therefore were prevented from upgrade to the high-grade Fe ores. If the externally derived, high salinity fluid percolated solely within the Saksaganskiy ore field it may be a useful vector to high-grade mineralization at great depths.

More research within the KRB is required in order to verify and fully understand the genetic relationship between the thrust zone, the iron ore enrichment and the high salinity fluids. Identification of the salt types within fluid inclusions and elemental analysis of an aqueous solution could constrain the origin and possible reservoirs of the high salinity fluids and further improve the genetic model. Future research should take into consideration a possible impact of the Saksaganskiy massif as a source of the fluid itself or as a heat source necessary to heat up the infiltrating basinal brines.

Acknowledgments

This article includes the results of PhD research projects undertaken by the main author Marta Sośnicka. It is based on her PhD thesis entitled: “Fluid types and their genetic meaning for the BIF belt formation, Krivoy Rog, Ukraine” at the AGH University of Science and Technology in Cracow, Poland under the supervision of Professor Adam Piestrzyński. This doctoral research benefited from Erasmus Scholarship no. ERAS/44/10–11 at the University of Leoben in Austria (2010/2011), the Dean Grant no. 15.11.140.205 at the Faculty of Geology, Geophysics and Environmental Protection (AGH, 2012) and the Swedish Institute Scholarship no. 382/00096/2012 (Visby Program for PhD studies in Sweden 2013) at Stockholm University in Sweden. MS is truly thankful to supervisor Prof. Adam Piestrzyński and all the people who strongly supported this research. Prof. Steffen Hagemann and Prof. Thomas Angerer are acknowledged for their critical and very insightful reviews.

Appendix A

Microthermometry data of type III fluid inclusions hosted by quartz vein 1 and 2, low-grade iron ore: morphologies, sizes (the longest diameters), presence of nahcolite crystals at 20 °C (nahc), homogenization temperatures of CO₂ phase–*T*_h(CO₂), melting temperatures of CO₂–clathrate–*T*_m(cla), and volume fractions of CO₂–*φ*(CO₂) at 20 °C.

Inclusion No.	Morphology	Size (μm)	nahc	<i>T</i> _h (CO ₂)/ °C	<i>T</i> _m (cla)/ °C	<i>φ</i> (CO ₂)
Ink11P1A5-1	cylindrical	30			8	0.16
Ink11P1A5-2	cylindrical, angular	27	+	4.5	8.3	0.14
Ink11P1A5-3	spherical	18		9	8.1	0.19
Ink11P1A5-4	cylindrical	13		8.5	8.3	0.25
Ink11P1A5-5	spherical	18	+	15	8.4	0.13
Ink11P1A5-6	negative crystal shaped	18		30.5	8.5	0.25
Ink11P1A1-1	negative crystal shaped	21		7	8.4	0.16
Ink11P1A1-2	negative crystal shaped	18		6.7	8.1	0.18
Ink11P1A1-3	cubical	16		6.9	8.3	0.13
Ink11P1A3-1	spherical	22		30	7.9	0.26

(continued)

Inclusion No.	Morphology	Size (μm)	nahc	<i>T</i> _h (CO ₂)/ °C	<i>T</i> _m (cla)/ °C	<i>φ</i> (CO ₂)
Ink11P1A3-2	cylindrical	59		-3.7	7.8	0.16
Ink11P1A3-3	negative crystal shaped	13			8.4	0.22
Ink11P1A6-1	negative crystal shaped	19		-0.1	7.9	0.17
Ink11P1A6-2	cylindrical, angular	23		2.7	7.8	0.16
Ink11P1A6-3	cubical	24		13.9	8.6	0.22
Ink11P1A4-1	cylindrical, angular	32			7.6	0.37
Ink11P1A4-2	spherical	28			8.1	0.68
Ink11P1A4-3	spherical	19			6	0.48
Ink11P1A7-1	spherical, angular	18		9.8	8.2	0.15
Ink11P1A7-2	cubical	21	+			0.28
Ink11P1A7-3	irregular	43			7.3	0.43
Ink11P1A7-4	spherical	12		12	8.3	0.14
Ink11P1A8-1	negative crystal shaped	15			8.2	0.31
Ink11P1A8-2	cylindrical, angular	12			8.1	0.17
Ink11P3A1-1	cylindrical	91	+			0.13
Ink11P3A1-2	negative crystal shaped	38		8.2	8.3	0.19
Ink11P3A1-3	spherical	21		10.6	8.3	0.28
Ink11P3A1-4	cylindrical, angular	39		7.6	8.4	0.15
Ink11P3A1-5	spherical, angular	30	+	28	8.3	0.17
Ink11P3A1-6	spherical	33		12.3	8	0.22
Ink11P3A1-7	negative crystal shaped	14		11.6	8.3	0.28
Ink11P3A1-8	spherical	20		12.1	8.3	0.19
Ink11P3A1-9	spherical	24		10.9	8.2	0.28
Ink11P3A1-10	spherical, angular	20	+	-1.3	8.2	0.16
Ink11P3A1-11	spherical, angular	17		25	8.2	0.25
Ink11P4A1-1	spherical, angular	31		-5.9	7.8	0.60
Ink11P4A1-2	cylindrical	24		-3.5	8.1	0.19
Ink11P4A1-3	cubical	15	+			0.15
Ink11P4A1-4	cubical	16		23	8.2	0.21
Ink11P4A1-5	irregular, angular	14				0.08
Ink11P4A2-1	irregular	28		10	8.1	0.51
Ink11P4A2-2	negative crystal shaped	17		10	8.1	0.42
Ink11P4A2-3	cylindrical, angular	29	+	2.8	8.1	0.15
Ink11P4A2-4	cylindrical	16		1.5	8.1	0.19
Ink11P4A3-1	irregular	28		-8	8.1	0.14
Ink11P4A3-2	irregular	16		-5.5	8.1	0.20
Ink11P4A3-3	negative crystal shaped	18		-10.4	8.2	0.15
K1F1-1	cylindrical	115	+	11.2	7.8	0.17
K1F1-2	irregular, angular	17	+			0.11
K1F1-3	cubical, angular	38		15	7	0.22
K1F1-4	spherical, angular	16		22.2	6.9	0.37
K1F1-5	cylindrical	26		11.8	7	0.22
K1F1-6	irregular	42		15.1	7.7	0.14
K1F1-7	spherical	29	+		7.9	0.07
K1F5-1	cylindrical	50		31	7.7	0.13
K1F2-8	irregular	45	+	23	7.7	0.19
K1F3-9	cylindrical	35	+	27.8	8.2	0.31
K1F1-10	irregular	68			8.2	0.18
K1F3-1	negative crystal shaped	61	+	21.8	7.9	0.20
K1F3-2	spherical	51		19.7	8	0.15
K1F3-3	spherical	27		17.5	8	0.24
K1F3-4	cylindrical	44	+			0.10
K1F3-5	spherical, angular	19				0.20
K1F3-6	cylindrical	32			7.9	0.35
K1F4-7	spherical, angular	58		27.5	7.6	0.17
K1F4-8	cylindrical	47		25	7.7	0.18
K1F4-9	negative crystal shaped	35		23.7	7.7	0.28
K1F4-10	spherical, angular	28		20.2	7.7	0.18
K1F4-11	cylindrical	25		18.5	7.8	0.20
K1F4-12	spherical	47		31	7.8	0.11
K1F5-13	negative crystal shaped	72		12.8	8	0.31
K1F5-14	cylindrical	64		16.3	7.7	0.25
K1F5-15	negative crystal shaped	49		14.7	7.7	0.22
K1F5-16	negative crystal shaped	26		14.6	7.7	0.28
K1FSR-1	irregular	73				0.26
K1F6-1	spherical	55	+	23.1	7.5	0.19
K1F6-2	irregular	62		20.5	7.8	0.18
K1F6-3	cubical, angular	49	+	30	7.7	0.19
K1F6-4	spherical, angular	27		22.1	7.6	0.18
K1F6-5	cylindrical, angular	38		22.2	7.7	0.19
K1F6-6	irregular	37		17.9	7.5	0.18
K1F6-7	cylindrical, angular	39		19.1	7.7	0.26
K1F6-8	cylindrical, angular	42		15.9	7.8	0.18
K1F7-1	spherical	43			8.2	0.15

Appendix B

Microthermometry data of type A fluid inclusions hosted by quartz vein, iron-rich quartzites: morphologies, sizes (the longest diameters), homogenization temperatures of CO₂ phase—*T_h*(CO₂), melting temperatures of CO₂—*T_m*(CO₂) and CO₂-clathrate—*T_m*(cla), volume fractions of CO₂—*φ*(CO₂) at 20 °C.

Inclusion No.	Morphology	Size (μm)	<i>T_h</i> (CO ₂)/ °C	<i>T_m</i> (CO ₂)/ °C	<i>T_m</i> (cla) / °C	<i>φ</i> (CO ₂)
QZ51pr-1	cylindrical	17	12.7	-57.1	9.3	0.20
QZ51pr-2	negative crystal shaped	14	14.9	-56.6	9.9	0.09
QZ51pr-3	negative crystal shaped	12	11.4		9.2	0.22
QZ51pr-4	irregular	12				0.20
QZ51pr-5	negative crystal shaped	9	17.2	-56.7	9.3	0.25
QZ51pr-6	cylindrical	9	15.3	-56.6	9.2	0.17
QZ51pr-7	spherical	6	16.9	-56.6	9.2	0.19
QZ51pr-8	cubic	6	15.9		9.3	0.31
QZ51pr-9	cylindrical	11	12.9		9.2	0.20
QZ51pr-10	irregular	19	16.3	-56.6	9.2	0.15
QZ51pr-11	cubic	7	15.7		9	0.17
QZ51pole3-1	irregular	25	12.5	-57.2	9.6	0.13
QZ51pole3-2	cylindrical	13	14.9	-56.6	8.9	0.20
QZ51pole3-3	cylindrical	17	13.5	-57.4	9.9	0.20
QZ51pole3-4	cylindrical	9	13.7	-56.6	9.9	0.19
QZ51pole4-5	cylindrical	12	13.8	-56.8	9.3	0.18
QZ51pole4-6	negative crystal shaped	8	16	-56.6	9.2	0.19
QZ51pole4-7	irregular	9	21.8		9.9	0.17
QZ51pole4-8	cubic	12	25.9	-56.6	8.9	0.29
QZ51pole4-9	cylindrical	10	12.4	-56.8	9.8	0.22
QZ51pole4-10	cubic	8	19.6	-58.1	9.9	0.19
QZ51pole4-11	cylindrical	12	12.9	-56.6	9.8	0.59
QZ51pole4-12	negative crystal shaped	8				0.31

Appendix C

Microthermometry data of type 1, type 2 and type 3 fluid inclusions hosted by quartz vein, thrust zone: morphologies, sizes (the longest diameters), presence of salt crystals at 20 °C (salt cryst), total homogenization temperatures *T_h*(LV → L), melting temperatures of ice—*T_m*(ice), decrepitation temperatures *T_D*, volume fractions of a vapor — *φ_{vap}* at 20 °C.

Inclusion No.	Type	Morphology	Size (μm)	Salt cryst	<i>T_h</i> / °C	<i>T_m</i> (ice)/ °C	<i>T_D</i> / °C	<i>φ_{vap}</i>
QBM811pole2zak-1	type1	cylindrical	15		285	-10.75	299	0.13
QBM811pole2zak-2		spherical	8		275	-8.85		0.16
QBM811pole2zak-3		irregular	11	+	281	-8.45		0.20
QBM811pole2zak-4		irregular	13			-8.75		0.12
QBM811pole2zak-5		negative crystal shaped	9			-8.85		0.16
QBM811pole2zak-6		cylindrical	8			-9.65		0.17
QBM811pole2zak-7		negative crystal shaped	15		239	-9.25		0.12
QBM811pole1-1		cylindrical	12		262	-10.95		0.13
QBM811pole1-2		cylindrical	9	+	261	-10.45		0.13
QBM811pole1-3		cylindrical	15					0.13
QBM811pole1-4		irregular	14		277	-10.15		0.11
QBM811pole1-5		irregular	25		279			0.15
QBM811pole1-6		spherical	6		263	-9.95		0.17
QBM811pole1-7		cylindrical	8			-9.05	299	0.14
QBM811pole1-8		cylindrical	13			-9.05	299	0.11
QBM811pole1-9		spherical	7		258	-10.05		0.13
QBM811pole1-10		cylindrical	6		262	-10.35		0.14

(continued)

Inclusion No.	Type	Morphology	Size (μm)	Salt cryst	<i>T_h</i> / °C	<i>T_m</i> (ice)/ °C	<i>T_D</i> / °C	<i>φ_{vap}</i>
QBM811pole1-11		cylindrical	8		264	-10.25		0.15
QBM811pole1-13		cylindrical	16	+		-9.45		0.07
QBM811pole1-14		cylindrical	10			-10.05		0.13
QBM811pole4-1		irregular	12	+		-11.35		0.15
QBM811pole4-2		irregular	15					0.15
QBM811pole4-3		cylindrical	11			-9.25		0.14
QBM811pole4-4		irregular	29	+				0.11
QBM811pole4-5		irregular	14					0.18
QBM811pole5-2		irregular	15			-11.45	294	0.15
QBM811pole5-3		cylindrical	12			-11.15	294	0.21
QBM811pole5-4		irregular	20					0.18
QBM811pole5-5		negative crystal shaped	7		274	-11.15		0.23
QBM811pole5-6		negative crystal shaped	9	+		-11.15	294	0.08
QBM811pole5-7		cylindrical	8		270	-10.55		0.20
QBM811pole5-8		irregular	11	+	281	-9.95		0.19
QBM811pole5-9		cylindrical	10					0.19
QBM811pole5-10		cylindrical	14			-10.95	266	0.16
QBM811pole5-11		cylindrical	10		274	-10.55		0.17
QBM811pole5-12		spherical, angular	5			-11.25	269	0.17
QBM811pole5-13		irregular	27			-11.25	269	0.11
QBM811pole5-14		irregular	22	+		-10.95	269	0.12
QBM811pole5-19		spherical, angular	8			-11.75	399	0.31
QBM9pole2i3-1		cylindrical	18	+	299	-9.95		0.20
QBM9pole2i3-2		cylindrical	9			-10.55		0.14
QBM9pole2i3-3		irregular	16			-9.95	299	0.13
QBM811pole5-18	type2	cylindrical	14		370	-11.25		0.19
QBM811pole5-1		cylindrical	17		324	-12.85		0.14
QBM811pole5-15		cylindrical	16		305	-11.75		0.16
QBM811pole5-16		cylindrical	10		304	-12.15		0.18
QBM8kaw2-1	type3	spherical	11		258	-3.95		0.32
QBM8kaw2-2		negative crystal shaped	10		256	-4.45		0.27
QBM8kaw2-3		negative crystal shaped	7		276	-4.45		0.20
QBM8kaw2-4		cylindrical	7		276			0.21

Appendix D

Results of Raman spectroscopy of the gas phases in fluid inclusions hosted by quartz vein (types 1, 2, 3) and quartz matrix of the breccia (Type 4), thrust zone.

Inclusion No.	Composition of a gas phase (mol%)			graphite/ <i>T_{cryst}</i>	Type
	CO ₂	CH ₄	N ₂		
QBM811pole1-1	-	8	92	-	type1
QBM811pole1-2	-	8.5	91.5	-	
QBM811pole4-1	-	2	98	+/506°C	
QBM811pole4-5	-	4	96	-	
QBM811pole4-3	8	3	89	-	
QBM811pole4-6	22	3	75	-	
QBM811pole5-20	-	4	96	-	
QBM811pole5-21	-	6	94	-	
QBM811pole1-15	100	-	-	+/598°C	
QBM811pole5-18	-	7	93	-	type2
QBM8kaw2-1	-	12	88	-	type3
QBM12-11	-	-	-	+/525°C	type4
QBM811pole4-7	98.8	0.2	1	-	CO ₂ -rich (near type1)
QBM8kaw2-6	99.1	-	0.9	-	CO ₂ -rich (near type3)
QBM8kaw2-5	100	-	-	-	CO ₂ -rich (near type3)

Appendix E

Results of microthermometry and Raman spectroscopy for CO₂–CH₄–N₂ (Type 5) fluid inclusions hosted by quartz clasts of the breccias, thrust zone: homogenization temperatures— $T_h(\text{car})$, melting temperatures— $T_m(\text{car})$, calculated molar volume V_M .

Inclusion No.	$T_h(\text{car})/^\circ\text{C}$	$T_m(\text{car})/^\circ\text{C}$	Composition, carbonic phase (mol%)			Density (g/cc)	V_M (cc/mole)	graphite/ T_{cryst}
			CO ₂	CH ₄	N ₂			
QBM12-1	-46.5	-61.1	97	2.1	0.9	1.072	40.381	
QBM12-2	-35.4	-61.9	97	2	1	1.030	42.050	
QBM12-3	-46.5	-60.7	97	2.2	0.8	1.072	40.376	
QBM12-4	-44.5	-61.1	96	3	1	1.058	40.639	
QBM12-5	-44.2	-61.9	96	3	1	1.057	40.684	
QBM12-6		-60.7	96	3	1			
QBM12-7		-60.7						+516°C

Appendix F

Summary of fluid inclusion microthermometric data in terms of FIAs: a number of measured fluid inclusions in a single FIA, averages and standard deviations for: $T_h(\text{car})$, $T_m(\text{cla})$, $T_m(\text{car})$, T_h , $T_m(\text{ice})$.

FIA No.	Number of measured FI	av. $T_h(\text{car})/^\circ\text{C}$	σ	av. $T_m(\text{cla})/^\circ\text{C}$	σ	av. $T_m(\text{car})/^\circ\text{C}$	σ	av. $T_h/^\circ\text{C}$	σ	av. $T_m(\text{ice})/^\circ\text{C}$	σ
<i>Fluid inclusions hosted by vein from the low-grade iron ore (Type III)</i>											
FIA1	6	13.5	9.14	8.3	0.17						
FIA2	3	6.9	0.12	8.3	0.12						
FIA3	3	13.2	16.85	8.0	0.26						
FIA4	3	5.5	6.05	8.1	0.36						
FIA5	3	-	-	7.2	0.90						
FIA6	4	10.9	1.10	7.9	0.45						
FIA7	2	-	-	8.2	0.05						
FIA8	11	12.5	7.98	8.3	0.10						
FIA9	5	4.5	13.09	8.0	0.17						
FIA10	4	6.1	3.95	8.1	0.00						
FIA11	3	-8.0	2.00	8.1	0.05						
FIA12	7	15.1	3.91	7.4	0.42						
FIA13	7	21.7	3.84	8.0	0.11						
FIA14	6	24.3	4.21	7.7	0.07						
FIA15	4	14.6	1.24	7.8	0.13						
FIA16	8	21.4	3.98	7.7	0.11						
FIA17	5	27.0	4.00	8.0	0.25						
<i>Fluid inclusions hosted by vein from the iron-rich quartzites (Type A)</i>											
FIA1	11	14.9	1.85	9.3	0.22	-56.7	0.18				
FIA2	4	13.7	0.85	9.6	0.41	-57	0.36				
FIA3	8	17.5	4.73	9.5	0.37	-56.9	0.54				
<i>Fluid inclusions hosted by quartz from the thrust zone (Types 1,2,3,4,5)</i>											
FIA1 (Type 1)	7							270	18.25	-9.2	0.72
FIA2 (Type 1)	13							266	7.28	-10.0	0.56
FIA3 (Type 1)	5							-	-	-10.3	1.05
FIA4 (Type 1)	14							275	3.96	-11.0	0.45
FIA5 (Type 1)	3							299	-	-10.2	0.28
FIA6 (Type 2)	4							326	26.76	-12.0	0.59
FIA7 (Type 3)	4							267	9.53	-4.3	0.24
FIA8 (Type 4)	2							283	0.0	-16.9	0.0
FIA9 (Type 5)	7	-43.4	4.12			-61.2	0.50				

Appendix G

Summary of fluid inclusion microthermometric data in terms of types: a number of measured FIAs within a type, averages and standard deviations for: $T_h(\text{car})$, $T_m(\text{cla})$, $T_m(\text{car})$, T_h , $T_m(\text{ice})$.

Host rock	FI host	Sample No.	FI type	No. of measured FIA's	av. $T_h(\text{car})/^\circ\text{C}$	σ	av. $T_m(\text{cla})/^\circ\text{C}$	σ	$T_m(\text{car})/^\circ\text{C}$	σ	av. $T_h/^\circ\text{C}$	σ	av. $T_m(\text{ice})/^\circ\text{C}$	σ
low-grade iron ore	quartz vein 1	Ink11	Type III aqueous-carbonic	11	8.3	10.1	8.1	0.4						
	quartz vein 2	K1	Type III aqueous-carbonic	6	20.4	5.5	7.7	0.3						
	quartz veins 1+2	Ink11+K1	Type III aqueous-carbonic	21	13.8	10.3	7.9	0.4						

(continued)

Host rock	Fl host	Sample No.	Fl type	No. of measured FIA's	av. T_h (car)/ °C	σ	av. T_m (cla)/ °C	σ	T_m (car)/ °C	σ	av. T_h / °C	σ	av. T_m (ice)/ °C	σ
iron-rich quartzites	quartz vein	QZ	Type A aqueous-carbonic	3	15.5	3.4	9.4	0.3	-56.8	0.4				
thrust zone	quartz vein+breccia	QBM	Types 1,2,3,4 aqueous	8							279	25	-10.1	2.1
	quartz breccia	QBM	Type 5 carbonic	1	-43.4	4.1			-61.2	0.5				

Appendix H

Summary of the fluid inclusion data in terms of fluid inclusion types, origin, minimum T_b , salinity and distinguished fluid types.

Host rock	Fl host	Sample No.	Fluid inclusion type	Origin	T_{min} / °C	Salinity (mass% NaCl equiv.)	Fluid type
low-grade iron ore	quartz veins 1, 2	Ink11, K1	Type I, carbonic	-	-	-	carbonic
			Type II, aqueous	-	-	-	early aqueous
			Type III, aqueous-carbonic	pseudo-secondary or/and secondary	231	2.46-7.21	low salinity $H_2O-CO_2(\pm N_2-CH_4)-NaCl(\pm NaHCO_3)$
	magnetite	Ink11, K1	Type IV, aqueous	-	-	-	late aqueous
			aqueous?	unknown	530	unknown	unknown
iron-rich quartzites	quartz vein	QZ	Type A, aqueous-carbonic	pseudo-secondary or/and secondary	219	0.003-1.98	$H_2O-CO_2(\pm N_2-CH_4)\pm NaCl$
thrust zone	quartz vein	QBM8, QBM9, QBM811	Type 1, aqueous	pseudo-secondary or/and secondary	239?	12.22-15.72	moderate salinity $H_2O-N_2-CH_4-NaCl(\pm CO_2, \pm C)$
			Type 2, aqueous	pseudo-secondary or/and secondary	304?	15.22-16.76	
			Type 3, aqueous	primary	256	6.38-7.1	low salinity $H_2O-N_2-CH_4-NaCl$
			CO ₂ -rich type	primary	-	-	$CO_2(\pm N_2-CH_4)$
		quartz breccia	QBM12	Type 4, aqueous	primary	283	20.11-35.0
high-grade iron ore	magnetite	MGF1, MGF6	Type 5, carbonic aqueous?	primary unknown	- 430-500	- unknown	$CO_2-CH_4-N_2(\pm C)$ unknown
iron quartzites	martite	MRF1	traces of fluid inclusions	remnants of primary fluid inclusions from replaced magnetite?	400 (very low intensity)	unknown	unknown

References

- Abramoff, M.D., Magalhaes, P.J., Ram, S.J., 2004. Image processing with ImageJ. *Biophoton. Int.* 11, 36–42.
- Angerer, T., Hagemann, S.G., Danyushevsky, L.V., 2012. Geochemical evolution of the banded iron formation-hosted high-grade iron ore system in the Koolyanobbing Greenstone Belt, Western Australia. *Econ. Geol.* 107, 599–64.
- Bakker, R.J., 1997. Clathrates: computer programs to calculate fluid inclusion V–X properties using clathrate melting temperatures. *Comput. Geosci.* 23, 1–18.
- Bakker, R.J., 1999. Adaptation of the Bowers and Helgeson (1983) equation of state to the $H_2O-CO_2-CH_4-N_2-NaCl$ system. *Chem. Geol.* 154, 225–236.
- Bakker, R.J., 2003. Package FLUIDS 1. Computer programs for analysis of fluid inclusion data and for modeling bulk fluid properties. *Chem. Geol.* 194, 3–23.
- Bakker, R.J., Diamond, L.W., 2006. Estimation of volume fractions of liquid and vapor phases in fluid inclusions, and definition of inclusions shape. *Am. Mineral.* 91, 635–657.
- Beane, R.E., 1983. The magmatic–meteoric transition. *Geothermal Resources Council, pp. 245–253 (Special Report no. 13).*
- Belevtsev, Ya.N., Belevtsev, R.Ya., Siroshtan, R.I., 1983. The Krivoy Rog Basin, chapter 5. In: Trendall, A.F., Morris, R.C. (Eds.), *Developments in Precambrian Geology, Iron-formation Facts and Problems vol. 6*. Elsevier Science Ltd., Amsterdam, pp. 211–249.
- Belevtsev, Ya.N., Kravchenko, V.M., Kulik, D.A., Belevtsev, R.Ya., Borisenko, V.G., Drozdovskaya, A.A., Epatko, Yu.M., Zankevich, B.A., Kalinichenko, O.A., Koval, V.B., Korzhnev, M.N., Kushyev, V.V., Lazurenko, V.I., Litvinskaya, M.A., Nikolayenko, V.I., Pirogov, B.L., Prozhogin, L.G., Pikovskiy, E.Sh., Samsonov, V.A., Skvortsov, V.V., Savchenko, L.T., Stebnovskaya, Yu.M., Tereshchenko, S.I., Chaykin, S.I., Yaroshchuk, M.A., 1991. Precambrian banded iron formations of the European part of the USSR. *Genesis of Iron-ores*. Naukova Dumka Press, Kiev (IGCP UNESCO Project, No 247 (in Russian)).
- Belykh, V.I., Dunai, E.I., Lugovaya, I.P., 2007. Physicochemical formation conditions of banded iron formations and high-grade iron ores in the region of the Kursk Magnetic Anomaly: evidence from isotopic data. *Geol. Ore Deposits* 49, 147–159.
- Beukes, N.J., Mukhopadhyay, J., Gutzmer, J., 2008. Genesis of high-grade iron ores of the Archaean iron ore group around Noamundi, India. *Econ. Geol.* 103, 365–386.
- Beyssac, O., Goffe, B., Chopin, C., Rouzaud, N., 2002. Raman spectra of carbonaceous material in metasediments: a new geothermometer. *J. Metamorph. Geol.* 20, 859–871.
- Bobrov, O.B., Gurskiy, D.S., Krasnozhan, M.D., Malyuk, B.I., Shcherbak, M.P., Kalinin, V.I., Bakarzhiev, A.H., Bugaenko, V.M., Esipchuk, K.Y., Geychenko, M.V., Galitskiy, V.V., Kyrylyuk, V.P., Kvasnytsa, V.M., Kvasnytsa, I.V., Kosovskiy, Y.O., Kozak, S.O., Kozar, M.A., Kravchenko, G.L., Kryvdyk, S.G., Kurlov, M.S., Koval, V.B., Klimenko, O.P., Lysenko, O.A., Lykov, L.I., Lysak, A.M., Makivchuk, O.F., Malykh, M.M., Mateyuk, V.V., Merkushev, I.E., Mudrovskaya, I.V., Nechaev, S.V., Nikolaevkiy, I.I., Pavlyshyn, V.I., Paranko, I.S., Prykhodko, V.L., Pogukaj, V.I., Ponomarenko, O.M., Indutniy, V.V., Isakov, L.V., Semka, V.A., Sergienko, V.M., Sivoronov, A.O., Skobelev, V.M., Stepanyuk, L.M., Strekozov, S.M., Sukach, V.V., Shvayberov, S.K., Zagnitko, V.M., Vysotskiy, B.L., Voloshyn, O.A., Turchanovskiy, I.M., Yaskevich, T.B., Kormakova, K.V., Stefanushyn, O.B., 2002. Main types of rock complexes and mineral deposits in the Ukrainian Shield, Geological Excursion Guidebook. International Symposium Organized by Ukrainian State Geological Survey, Ukrainian State Geological Research Institute, Ukrainian National Academy of Sciences, European Program “Ore Deposits Geodynamics” (GEODE), Kiev, Ukraine, September 13–26, 2002. Ukrainian State Geological Survey, Kiev.
- Bodnar, R.J., 2003. Reequilibration of fluid inclusions. In: Samson, I., Anderson, A., Marshall, D. (Eds.), *Fluid Inclusions: Analysis and Interpretation. Short Course Volume 32*. Mineralogical Association of Canada, pp. 213–230.

- Bowers, T.S., Helgeson, H.C., 1983. Calculation of thermodynamic and geochemical consequences of nonideal mixing in the system H_2O-CO_2-NaCl on phase relations in geologic system: equation of state for H_2O-CO_2-NaCl fluids at high pressures and temperatures. *Geochim. Cosmochim. Acta* 47, 1247–1275.
- Burlinson, K., 1988. An instrument for fluid inclusion decrepitation and examples of its application. *Bull. Mineral.* 111, 267–278.
- Burlinson, K., 2008. An updated understanding of the baro-acoustic decrepitation method. Second Asian Current Research on Fluid Inclusions Meeting (ACROFI-II), Kharagpur, India, 12–14 November 2008 (<http://www.appliedminex.com/decrep/orals/adexplain.htm>).
- Diamond, L.W., 2003. Introduction to gas-bearing, aqueous fluid inclusions. In: Samson, I., Anderson, A., Marshall, D. (Eds.), *Fluid Inclusions: Analysis and Interpretation*. Short Course Volume 32. Mineralogical Association of Canada, pp. 101–158.
- Duuring, P., Hagemann, S.G., Novikova, Y., Cudahy, T., Laukamp, C., 2012. Targeting iron ore in banded iron formations using ASTER data: weld range Greenstone Belt, Yilgarn Craton, Western Australia. *Econ. Geol.* 107, 585–597.
- Faure, G., Mensing, T.M., 2005. *Isotopes: Principles and Applications*. 3rd edition. John Wiley & Sons, Inc., Hoboken, New Jersey, USA.
- Figueiredo e Silva, R.C., Hagemann, S., Lobato, L.M., Carlos Alberto Rosière, C.A., Banks, D.A., Davidson, G.J., Vennemann, T., Hergt, J., 2013. Hydrothermal fluid processes and evolution of the Giant Serra Norte Jaspilite-hosted iron ore deposits, Carajás Mineral Province, Brazil. *Econ. Geol.* 108, 739–779.
- Goldstein, R.H., Reynolds, T.J., 1994. Systematics of fluid inclusions in diagenetic minerals. *SPEM Short Course Vol. 31*. SPEM (199 pp.).
- Hagemann, S.H., Rosière, C.A., Lobato, L., Baars, F., Zucchetti, M., Figueiredo e Silva, R.C., 2006. Controversy in genetic models for Proterozoic high-grade, banded iron formation (BIF)-related iron deposits – unifying or discrete model(s)? *Appl. Earth Sci. (Trans. Inst. Min. Metall. B)* 115, 147–151.
- Hollister, L.S., 1990. Enrichment of CO_2 in fluid inclusions in quartz by removal of H_2O during crystal-plastic deformation. *J. Struct. Geol.* 12, 895–901.
- Hoshino, K., Nagatomi, A., Watanabe, M., Okudaira, T., Beppu, Y., 2006. Nahcolite in fluid inclusions from Ryoke metamorphic rocks and its implication for fluid genesis. *J. Mineral. Petrol. Sci.* 101, 254–259.
- Janousek, V., Farrow, C.M., Erban, V., Trubac, J., 2011. Brand New Geochemical Data Toolkit (GCDKit 3.0) – Is It Worth Upgrading and Browsing Documentation? (Yes!). *Geologicke vyzkumy na Morave a ve Slezsku* 18, pp. 26–30.
- Kalinichenko, O.A., 1992. Geologo-geochemicheskiye osobennosti stroyeniya i formirovaniya glubinnih zon okslenia Krivorozhskovo Basena w svyazi z otsenкой ich rudonosnosti na glubinu. PhD Dissertation, Dnipropetrovsk, Ukraine, Dnipropetrovsky Gorny Institut Imenia Artema (in Russian), unpublished PhD Thesis.
- Kalyayev, G.I., Glevasskiy, Ye.B., Dimitrov, G.Kh., 1984. *Paleotektonika i stroyeniye zemnoy kory dokembriyskoy zhelezorudnoy provintsii Ukrainy*. Nauk. Dumka, Kiev (240 pp., in Russian).
- Khudur, D., 2006. *Geologiya Saksaganskogo nadviga Krivorozhskoy Struktury i yego rol v formirovaniy zalezhey bogatykh zheleznykh rud*, PhD Dissertation, Dnipropetrovsk, Ukraine, Ministerstvo Obrazovaniya i Nauki Ukrainy Natsionalny Gorny Universitet (in Russian), unpublished PhD Thesis.
- Kulik, D.A., Korzhnev, M.N., 1997. Lithological and geochemical evidence of Fe and Mn pathways during deposition of Lower Proterozoic banded iron formation in the Krivoy Rog Basin (Ukraine). In: Nicholson, K., Hein, J.R., Bühn, B., Dasgupta, S. (Eds.), *Manganese Mineralization: Geochemistry and Mineralogy of Terrestrial and Marine Deposits*. Geological Society Special Publication, London 119, pp. 43–80.
- Lazarenko, E.K., Gerschoyg, Yu.G., Butschinskaya, N.I., Belevtsev, R.Ya., Voznyak, D.K., Galaburda, Yu.A., Galiy, S.A., Kvasnitsa, V.N., Kulchitskaya, A.A., Melnik, Yu.P., Melnikov, V.C., Pavlishin, V.I., Pirogov, B.L., Turkyevich, G.I., 1977. *Mineralogy of the Krivoy Rog Basin*. Naukova Dumka, Kiev (544 pp., in Russian).
- Paranko, I.S., 1993. Nyektorye osobennosti geologicheskogo razvitiya Krivorozhskoy struktury. *Geol. Zh.* 4, 112–133 (in Russian).
- Paranko, I.S., 1997. Ryadi stratifikovanih formatsiy i formatsiyni tipi proterozoyskikh metamorfichnikh kompleksiv Ukrainского shchita. Avtoref. dis. doktora geol. Nauk., Lviv (35 pp. (in Russian)).
- Paranko, I.S., Butyrin, V.K., 2004. Razlomno-blokovaya tektonika Krivorozhskoy struktury. *Geol. Mineral. Visnik* 1 (11), 5–13 (in Russian).
- Paranko, I.S., Mikhnitskaya, T.P., 1991. Etapy geologicheskogo razvitiya i stratigrafiya Krivorozhskoy Struktury. Preprint 91–10, 1–51, Akademia Nauk Ukrainy Institut Geologicheskikh Nauk, Kiev (in Russian).
- Paranko, I.S., Butyrin, V.K., Zmiyevskiy, G.Ye., Pinskaya, A.A., 1992. Gosudarstvennaya geologicheskaya karta Krivorozhskogo gornorudnogo rayona, mashtab 1:50 000. Krivorozhskaya gruppa listov (M-36-139-B,G; M-36-140-A,B; L-36-8-A), Obyasnitelnaya zapiska. Goskomgeologii Ukrainy, Kiev (220 pp. (in Russian)).
- Paranko, I.S., Yevtekhov, V.D., Meddakh, R., 1993. K voprosu o formatsionnoy i stratigraficheskoy prinadlezhnosti talkovykh porod Krivorozhskoy struktury. KGRI, Krivoy Rog (16 pp. – Dep. v GNTB Ukrainy, No2077-Uk93 (in Russian)).
- Paranko, I.S., Butyrin, V.K., Kozar, M.A., 2005. Do pitannya pro stratigrafichne rozchlenuvannya metavulkanogenno-osadovikh vidkladiv Krivorozhskoy struktury. *Mineralnye Resursy Ukrainy* 3, pp. 35–40 (in Russian).
- Paranko, I.S., Burman, L., Yarko, S., 2011. *Mineralno-syryevoy potentsial Ukrainy*. Krivoy Rog, Izdatelskiy Dom (332 pp. (in Russian)).
- Perry, E.C., Ahmad, S.N., 1981. Oxygen and carbon isotope geochemistry of the Krivoy Rog iron formation Ukrainian SSR. *Lithos* 14, 83–92.
- Pieczonka, J., Piestrzyński, A., Paranko, I.S., 2011. *Geology of Selected Ukrainian Deposits of Mineral Resources*. Publishing house of AGH, Cracow, Poland (157 pp., in Polish).
- Ramsay, J.G., 1980. The crack-seal mechanism of rock deformation. *Nature* 284, 135–139.
- Reshetnyak, V.V., 1993. Glubinnoye geologicheskoye stroyeniye Krivorozhskogo zhelezorudnogo basseyna i perspektivy yego rudonosnosti. PhD Dissertation, Kiev (in Russian), unpublished PhD Thesis.
- Robb, L., 2005. *Introduction to Ore-forming Processes*. Blackwell Publishing, Oxford, UK.
- Roedder, E., 1984. Fluid inclusions. *Reviews in Mineralogy* vol. 12. Mineralogical Society of America, Washington D.C.
- Rosière, C.A., Rios, F.J., 2004. The origin of hematite in high-grade iron ores based on infrared microscopy and fluid inclusion studies: the example of the Conceição mine, Quadrilátero Ferrífero, Brazil. *Econ. Geol.* 99, 611–624.
- Semenenko, N.P., 1978. *Zhelezisto-kremnistyye formatsii Ukrainского Shchita* vol. 2. Naukova Dumka, Kiev (368 pp., in Russian).
- Shcherbak, M.P., Bobrov, O.B. (Eds.), 2005. *Mineral Deposits of Ukraine. Metalliferous Mineral Deposits vol. 1*. Centre of Europe Publishing House, State Geological Survey of Ukraine, National Academy of Sciences of Ukraine, Kyiv-Lviv (783 pp. (in Russian)).
- Spier, C.A., Barros de Oliveira, S.M., Rosière, C.A., Ardisson, J.D., 2008. Mineralogy and trace-element geochemistry of the high-grade iron ores of the Águas Claras Mine and comparison with the Capão Xavier and Tamandua iron ore deposits, Quadrilátero Ferrífero, Brazil. *Mineral. Deposita* 43, 229–254.
- Stepanyuk, L.M., Bobrov, A.B., Zakharov, V.V., et al., 2010. Vremya formirovaniya granitoidov saksaganskogo kompleksa. *Mineralnye Resursy Ukrainy* 1, pp. 21–26 (in Russian).
- Thorne, W., Hagemann, S., Vennemann, T., Oliver, N., 2009. Oxygen isotope compositions of iron oxides from high-grade BIF-hosted iron ore deposits of the Central Hamersley Province, Western Australia: constraints on the evolution of hydrothermal fluids. *Econ. Geol.* 104, 1019–1035.
- Tödheide, K., Franck, E.U., 1963. Das Zweiphasengebiet und die kritische Kurve im System Kohlendioxid – Wasserbis zu Drucken von 3,500 bar. *Z. Phys. Chem. Neue Folge* 37, 387–401.
- Winter, J.D., 2001. *An introduction to Igneous and Metamorphic Petrology*, Upper Saddle River, New Jersey.
- Yesipchuk, K.Yu., Bobrova, O.B., Stepanyuk, L.M., et al., 2004. Korrelyatsionna khronostratigraficheskaya skhema rannego dokembriya Ukrainского shchita. *UkrDGRI, Kiev* (90 pp. (in Russian)).
- Yevtekhov, V.D., Paranko, I.S., 1996. Proyavleniye metasomatoza v stratigraficheskikh podrazdeleniyakh Krivbassa. *Sovremennyye problemy geologii i mineralogii zhelezisto-kremnistykh formatsiy i ikh obramleniya*. Izd-vo KTU, Krivoy Rog, pp. 63–64 (in Russian).